Fabrication and Modelling of Vertically Aligned Carbon Nanotube Composites for Vibration Damping

by

JIA, Jiangying

A Thesis Submitted in Partial Fulfillment

of the Requirements for the Degree of

Master of Philosophy

in

Mechanical & Automation Engineering

The Chinese University of Hong Kong

September 2009

Thesis/Assessment Committee

Professor Li, Wen Jung (Chair)

Professor Liao, Wei Hsin (Thesis Supervisor)

Professor Du, Ruxu (Committee Member)

Professor Ricky Lee (External Examiner)

ABSTRACT

In this research, high density aligned multi-walled carbon nanotubes (CNTs) and the CNT/epoxy composites are fabricated. To predict the energy dissipation in these composites, a structural damping model of composite unit cell composed of resin, sheath and nanotube is developed. The resin is described as viscoelastic material using Maxwell model and three-parameter standard solid model, respectively. The CNT/epoxy composite is modeled based on the "stick-slip" mechanism, to describe the load transfer behavior between the CNT and its sheath. In order to further study the damping mechanism of the CNT composite, key parameters, such as length, center-to-center distance and critical stress of CNTs that are expected to affect the composite damping performances are studied. The simulation results show that loss factor of the CNT composite with varying parameters is sensitive to the applied stress.

摘要

在本研究中，作者制備了高密度排列的多壁碳納米管 (CNTs) 和碳納米管/環氧樹脂複合材料。爲了更加深入的研究該複合材料能量耗散機理，作者構建了一個包含單段碳納米管的複合材料結構單元模型進行剖析。這個複合材料結構單元模型是由樹脂，外鞘和納米管組成。在這項研究中，樹脂被類比成粘彈性材料，分別採用麥克斯韋模型和三參數標準模型進行建模。碳納米管/環氧樹脂複合模型是在“粘-滑”機理的基礎上進行模擬，來描述碳納米管及其鞘之間負荷轉移的行爲。爲了進一步研究碳納米管複合材料的阻尼機理，那些預計會影響碳納米管/環氧樹脂複合材料阻尼性能的關鍵參數，如碳納米管的長度，中心對中心距離和臨界應力，分別進行了研究。仿真結果表明，上述關鍵參數的變化會導致碳納米管複合材料的損耗因子產生變化。

ACKNOWLEDGEMENTS

My deepest gratitude goes to my supervisor, Professor Liao Wei-Hsin (廖維新教授), for his insight, invaluable guidance throughout my entire study and his patience in teaching me scientific methods to carry out research.

I would like to express my appreciation to Prof. Du Ruxu (杜如虛教授), Prof. Li Wen Jung (李文榮教授), and Prof. Ricky Lee (李世瑋教授) for serving as my committee members and providing comments on this research.

I am grateful to the technicians in the NFF Lab, HKUST who helped me to solve many practical problems encountered in the fabrication of samples. In my group, my sincere thanks are to Dr. Chan Kwong Wah (陳光華博士), Mr. Chen Chao (陳超先生), Mr. Chen Jinzhou (陳金舟先生), Mr. Cheung Wai Ming (張偉明先生), Mr. Guo Hongtao (郭洪濤先生), and Mr. Liang Junrui (梁俊睿先生). Their co-operation and sharing have made my MPhil study enjoyable and memorable.

Finally and most importantly, I feel a deep and sincere gratitude for my parents, Mr. Jia Jin (賈進先生), Mrs. Zhan Jihong (詹繼紅女士) and my boyfriend, Mr. Yue Zhongli (岳中力先生), whose endless support and encouragement have been a source of inspiration that led to the completion of this thesis.

TABLE OF CONTENTS

LIST OF FIGURES

LIST OF TABLES

CHAPTER ONE

INTRODUCTION

This chapter presents background knowledge and related literature reviews on vibration damping and carbon nanotube composites. The basic knowledge of vibration damping and damping materials are also provided. The fabrication processes about carbon nanotubes and carbon nanotube composites are introduced. Recent researches on carbon nanotube composites are reviewed. At the end of this Chapter, the research objective and organization of this thesis are introduced.

1.1 Background

1.1.1 Vibration damping

Over a wide range of engineering applications—from transportation, through manufacturing, to infrastructure—there is an ever-increasing demand to reduce mechanical vibration and noise. Reduced vibration and noise would result in an improved environment for human beings. Additionally, machines and structures operating under lower stress levels will generally offer better performance and a longer operating life.

Unfortunately, the suppression of noise and vibration is made increasingly difficult by concomitant requirements to reduce weight. Weight reduction in machines and structures can produce both performance and economic benefits. However, cutting down on weight invariably points towards the adoption of thin-walled fabrications, which are flexible and have low natural frequencies. Resonances that occur at these low frequencies are notoriously difficult to control using conventional technologies.

At the most fundamental level, in thin-walled structures, damping is introduced by bonding a viscoelastic layer to the host structure. Viscoelastic materials usually comprise long-chain molecules, which are effective at converting mechanical energy into heat when deformed. If a single viscoelastic layer is applied to the host structure then this is known as a free-layer (or 'unconstrained') treatment. If a second layer, generally of metallic material, is bonded to the viscoelastic material then energy dissipation can be dramatically increased. In its basic form, this latter type of fabrication is known as a passive constrained-layer damping (PCLD) treatment.

Passive vibration damping is one of the most commonly used vibration control approaches. In a passive system, no control or feedback action is applied to the system and the system design is fixed. Passive damping materials/mechanisms are used in the structures in order to absorb/dissipate energy. Usually, the damping capacity is quantified by using 'loss factor', which represents the ratio of energy dissipation over total system energy input over a cycle.

Damping material plays an important role in passive vibration damping system. Vibration can be reduced via damping materials by transferring the kinetic energy into heat. One of the widely used passive damping materials is viscoelastic materials. Viscoelasticity, also known as anelasticity, describes materials that exhibit both viscous and elastic characteristics when undergoing plastic deformation. Viscous materials resist shear flow and strain linearly with time when stress is applied. Elastic materials strain instantaneously when stretched and just as quickly return to their original state once the stress is removed. Viscoelastic materials have elements of both of these properties and, as such, exhibit time dependent strain.

Conventional damping treatments are based on viscoelastic and elastomeric materials. These materials show promise for energy dissipation; however structural integrity issues associated with integration into composite systems present significant challenges. For example, during the composite cure cycle conventional damping films experience severe loss in performance at elevated temperatures (above 60℃) due to resin penetration [Brackbill et al., 2000; Biggerstaff et al., 1998] and poor thermal stability of the viscoelastic polymer. Another limitation of traditional damping films is that they can not be used to reinforce the stiffness of the composite structure. This is

because large strains must be engineered in the damping film to create energy dissipation, which necessitates a soft material. In order to overcome these limitations, there is a need to explore novel materials for structural damping and stiffness augmentation in composite structures.

1.1.2 Carbon nanotubes

The discovery of multi-walled carbon nanotubes (MWNTs) in 1991 [Iijima, 1991] has stimulated ever-broader research activities in science and engineering devoted to carbon nanotube structures and their applications. This is due in large part to the combination of their expected structural perfection, small size, low density, high stiffness, high strength (the tensile strength of the outer most shell of MWNT is approximately 100 times greater than that of aluminum), and excellent electronic properties. As a result, carbon nanotubes (CNTs) may find use in a wide range of applications in material reinforcement, field emission panel display, chemical sensing, drug delivery, and nanoelectronics.

Generally, there are two main types of carbon nanotubes that can have high structural perfection. Single-walled nanotubes (SWNTs) consist of a single graphite sheet seamlessly wrapped into a cylindrical tube (Figure 1.1-1, A to D). Multi-walled nanotubes comprise an array of such nanotubes that are concentrically nested like rings of a tree trunk (Figure 1.1-1 E).

Despite structural similarity to a single sheet of graphite, which is a semiconductor with zero band gap, SWNTs may be either metallic or semiconducting, depending on

the sheet direction about which the graphite sheet is rolled to form a nanotube cylinder. This direction in the graphite sheet plane and the nanotube diameter are obtained from a pair of integers (n, m) that denote the nanotube type. Depending on the appearance of a belt of carbon bonds around the nanotube diameter, the nanotube is either of the armchair (n=m), zigzag (n=0 or m=0), or chiral (any other n and m) variety. All armchair SWNTs are metals; those with n-m=3k, where k is a nonzero integer, are semiconductors with a tiny band gap; and all others are semiconductors with a band gap that inversely depends on the nanotube diameter. The electronic properties of perfect MWNTs are rather similar to those of perfect SWNTs, because the coupling between the cylinders is weak in MWNTs.

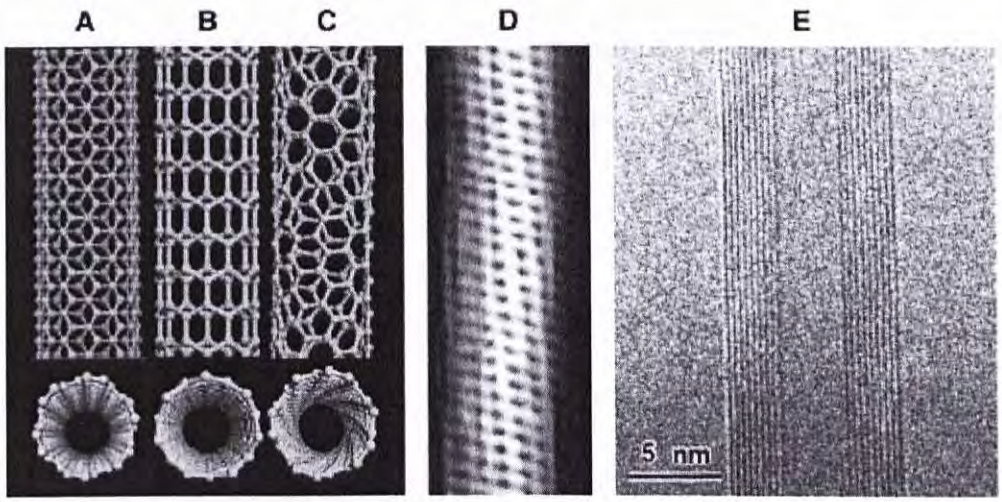

Figure 1.1-1 Schematic illustrations of CNTs structures

3D models of armchair(A), zigzag(B), and chiral SWNTs (C). SEM image of the helical structure of a chiral SWNT(D). TEM image of a MWNT (E) ([Baughman, 2002])

The mechanical properties of CNTs are closely related to the nature of the bonds between the carbon atoms. The bonding mechanism in a carbon nanotube structure is similar to that of graphite, since a CNT can be thought of as a roll-up grapheme sheet.

The atomic number for carbon is 6, and the atom electronic structure is $1s^2 2s^2 2p^2$ in atomic physics notation. When carbon atoms combine to form graphite, sp^2 hybridization occurs. In this process, one s-orbital and two p-orbitals combine to form three hybrid sp^2 -orbitals at 120° to each other within a plane (Figure 1.1-2). This in-plane bond is referred to as a σ -bond. This is a strong covalent bond that binds the atoms in the plane, and results in the high stiffness and high strength of a CNT. The remaining p-orbital is perpendicular to the plane of the σ -bond. It contributes mainly to the interlayer interaction and is called the π -bond. These out-of-plane, delocalized π -bonds interact with the π -bonds on the neighboring layer. This interlayer interaction of atom pairs on neighboring layers is much weaker than a σ -bond. For instance, in the experimental study of shell-sliding [Yu et al., 2000], it was found that the shear strength between the outermost shell and the neighboring inner shell was 0.08 MPa and 0.3 MPa according to two separate measurements on two different MWNTs.

Due to high-strength covalent carbon-carbon bonds, carbon nanotubes have many excellent properties. For example, the predicted elastic moduli of single-walled nanotubes are greater than 1 TPa and the predicted tensile strengths are of the order of 100 GPa. A multi-walled carbon nanotube was tested to have a tensile strength of 63 GPa. In comparison, high-carbon steel has a tensile strength of approximate 1.2 GPa. These exceptional properties have been substantiated by a variety of experimental procedures [Salvetat el al., 1999; Treacy et al., 1996; Wong et al., 1997].

The unique electrical and mechanical properties of carbon nanotubes make them of potential use in nanotechnology engineering. One essential prerequisite for realizing

this goal is to be able to grow nanotubes at controlled sites, in predetermined orientations and to form interconnections. Techniques have been developed to produce nanotubes in sizeable quantities, including arc discharge, laser ablation, high pressure carbon monoxide (HiPCO), and chemical vapor deposition (CVD). Most of these processes take place in vacuum or with process gases. CVD growth of CNTs can occur in vacuum or at atmospheric pressure. Large quantities of nanotubes can be synthesized by these methods; advances in catalysis and continuous growth processes are making CNTs more commercially viable.

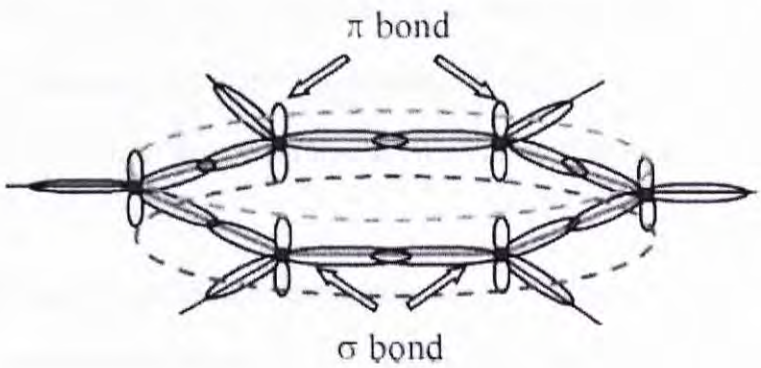

Figure 1.1-2 Basic hexagonal bonding structure for one graphite layer (the grapheme sheet)
Carbon nuclei shown as filled circles, out-of-plane π -bonds represented as delocalized (dotted line), and σ -bonds connect the C nuclei in-plane ([Qian, 2002])

Significant progress in growing aligned carbon nanotube films has been made recently with a combined approach of pre-catalyst patterning and chemical vapor deposition (CVD). CVD is widely used for this purpose due to its advantages of growing nanotubes on pre-patterned catalysts on planar substrates such as Si. One and two-dimensional connections and/or junctions with nanotubes have been fabricated by *in situ* growth processing and subsequent nanofabrication.

1.1.3 Fabrication of carbon nanotube composites

Carbon nanotube/epoxy composites have been widely investigated in the last decade since CNT/thermosetting resin composites were first fabricated in 1994 [Ajayan et al., 1994]. CNTs are considered to be the ideal reinforcing materials for making polymer composites due to their large specific surface area and aspect ratio, high tensile strength and Young's modulus, and superior thermal and electrical properties. However, the mechanical and physical properties of CNT polymer composites are much lower than the predicted values. The critical issues for achieving desirable properties of the CNT/polymer composites are to introduce a high content of CNTs with uniform dispersion and controlled alignment throughout the polymer matrix and improve CNT/epoxy interface properties [Moniruzzaman et al., 2006].

High-strength epoxy resins are commonly used polymers in the formation of CNT/epoxy composites that can serve as multifunctional materials with light weight, high strength, and high electrical conductivity for many industrial applications, such as aircrafts and electronic products. Depending on the chemical compositions and curing kinetics of the epoxy resins, it is possible to vary their mechanical properties such as Young's modulus, strength, and hardness, and physical properties such as thermal conductivity and electrical conductivity. Epoxy resins start in a liquid form to facilitate dispersion of CNTs. Afterwards, the mixture of CNTs and epoxy resins is cured when a hardener or agent is added to form a solid-state CNT/epoxy composite. There are many methods to disperse CNTs in epoxy resins for preparing CNT/epoxy composites, such as blending [Gojny et al., 2005], solution mixing [Zhu et al., 2004], and buckypaper-based processing [Wang et al., 2004]. Blending is a direct method to mix CNTs with epoxy resins by high shear forces or ultrasonication. The

disadvantages of blending are that CNTs can not be effectively dispersed in epoxy resins and CNT content is limited due to the high viscosities of the epoxy resins at higher CNT contents. Solutions mixing is the most common method as it can facilitate better dispersion of CNT in epoxy resins. This method generally involves dispersion and mixing of CNTs and epoxy in a suitable solvent by mechanical stirring, magnetic agitation, or high-energy sonication, followed by controlled evaporation of the solvent. The dispersion of CNTs can be improved by adding surfactants or modifying CNTs by chemical functionalization. However, the chemical modification process may destroy the structure of the CNTs and decrease both the Young's modulus and tensile strength, and the distribution of CNTs in epoxy resins may become inhomogeneous during slow solvent evaporation. Besides the dispersion issue, the rapidly increasing viscosity of the epoxy resin makes it difficult to achieve higher CNTs content in the composites. The buckypaper based processing is a new method to fabricate CNT/epoxy composites with a high content of single-walled CNTs, which involves the infiltration of an epoxy resin from solution into buckypaper members as a pre-existing CNT network. Buckypaper membranes were generally made through multistep dispersion and micro-filtration of a suspension of CNTs, which is time consuming. CNTs in the buckypaper membranes are randomly oriented, so the mechanical and physical properties of the CNT/epoxy composites might not be desirable.

CNT/epoxy composites fabricated by the methods mentioned above can not yield significant improvements in composite performance because effective dispersion and controlled orientation of a high CNT content in the epoxy resin matrix can not be

achieved. As a result, it is demanding to find out how to stack aligned and continuous CNT sheets to form a CNT perform for preparing CNT/polymer composites.

1.1.4 Literature review on carbon nanotube composites

New fabrication techniques have enhanced the production of CNTs [Chiang et al., 2001], leading to the possibility that lightweight structural polymers with excellent mechanical properties can be produced using small weight/volume fractions of CNTs. Experimental results also demonstrated that the improvement of material properties relies on nanotube dispersion and resin/nanotube interfacial bonding [Thostenson et al., 2001]. However, unlike conventional fiber-reinforced composites, CNT-based composites have fillers of the same length scale as polymer chains, and the interaction mechanisms between nanotubes and polymers are affected by interfacial chemical bonds, Van der Waals forces, and mechanical interlock. To understand such mechanism, molecular dynamics (MD) methods are often used [Odegard et al., 2001]; however, for large and complex systems, MD simulations require expensive computational facilities as well as extensive computation time. On the other hand, continuum mechanics can provide comparable results with less computation effort [Ru, 2000].

For CNT-based composites, relatively little attention has been given to their energy-dissipating mechanisms. Previous research has explored the effects of nano-scale particle fillers on the damping properties of polymer composites. For elastomeric materials, it has been found that rod-like aggregates of roughly spherical carbon black particles increase the material damping in the strain range in which the breakdown

and reformation of carbon black aggregates occurs. This strain-dependent damping enhancement is known as the Payne effect. Such analogous improvement in energy loss is expected in composites containing CNT fillers. Furthermore, because of the small size of nanotubes, the surface area to mass ratio (specific area) of CNTs is extremely large. It is anticipated that significant energy dissipation can be achieved by taking advantage of the weak bonding and interfacial friction between individual CNTs and resin. While a promising damping ability of a densely packed CNT thin film was observed [Koratkar et al., 2003], damping characteristics of CNT filled composites have not been investigated in detail. To understand energy loss associated with CNTs, Buldum and Lu found that a nanotube first sticks and then slips suddenly when the force exerted on it is sufficiently large [Buldum et al., 1999]. The resulting hysteresis observed in the plot of force versus distance provided the energy dissipated. By using an AFM tip applied to pyrolytic graphite, Holscher et al. also observed that the tip moves in a "stick-slip" manner over the surface [Holscher et al., 1998].

Based on the "stick-slip" phenomenon previously observed at the atomic scale on graphite surface, structural damping models of CNT-based composites have been developed by applying this "stick-slip" motion to the nanotube/resin interface [Zhou et al., 2003]. Zhou et al. [2003] first developed a "stick-slip" damping model for composites containing well-dispersed individual SWNTs and performed damping measurements on CNT-based composites. Analytical and theoretical results showed a strain-dependent damping enhancement due to "stick-slip" motion at the interface of the SWNTs and the resin. Following Zhou et al.'s effort, Liu et al. [2006] presented an analysis on the structural damping characteristics of polymeric composites containing nanoropes. The SWNT rope was modeled as a closed-packed lattice

consisting of seven nanotubes in hexagonal array. The resin was described as a viscoelastic material using two models: Maxwell model and three-element standard solid model. The composite was modeled as a three-phase system consisting of a resin, a resin sheath acting as a shear transfer zone, and SWNT ropes. The "stick-slip" mechanism was proposed to describe the load transfer behavior between a nanorope and a sheath and between individual SWNTs. The analytical results indicated that the loss factor of the composite is sensitive to stress magnitude. It was illustrated that the "stick-slip" friction is the main contribution for the total loss factor of CNT-based composites even with a small amount of nanotubes/ropes.

Dai and Liao [2007] developed models for CNT composite by using the "stick-slip" mechanism in order to study the damping mechanism. Other than analytical model, a FEM based composite unit cell model was built and solved. Under the shear loading, simulation was carried out to investigate surface sliding status between CNT and epoxy matrix under different strain level and CNT orientation. Loss factor can be obtained from the ratio of energy dissipation out of energy input.

1.2 Research Objective

This research is aimed to study the damping effect caused by CNT addition. Detailed procedures for fabricating vertically aligned multi-walled CNTs and the CNT/Epoxy composites are given. Although a limited number of studies have attempted to develop models for nanotube-reinforced polymer composites in order to describe their mechanical behaviors, these studies have not been applied to vertically aligned carbon nanotube composites so far.

In order to study the damping mechanism of the fabricated composite with vertically aligned multi-walled CNTs, models for the CNT composite are developed. A structural mechanics based composite unit cell model is built and analyzed. The developing process of sliding surface between CNT and base epoxy matrix is taken into consideration. Under the uniaxial loading, loss factors can be obtained from the ratio of energy dissipation out of energy input per cycle.

Based on the structural damping model, further parametric studies are performed. Several parameters such as CNT segment length, CNT center-to-center distance, and critical stress are discussed with respect to composite damping capacity (loss factor).

1.3 Thesis Organization

This thesis consists of five chapters. In Chapter One, background and literature review on related research are introduced. In Chapter Two, details about fabricating vertically aligned multi-walled CNTs and the CNT/epoxy composites are given. In Chapter Three, a structural mechanics based model of a composite unit cell is developed. Energy loss under uniaxial loading is calculated. In Chapter Four, numerical examples on parametric studies are given. Several parameters are studied. A range of parameters with respect to damping performance is discussed. Finally in Chapter Five, conclusion and future work are given.

CHAPTER TWO

FABRICATION OF CNT AND CNT/EPOXY COMPOSITES

In this chapter, a detailed procedure for fabricating multi-walled carbon nanotube film is firstly given. High-density aligned multi-walled carbon nanotube film is prepared on the silicon/silicon dioxide substrate using a plasma-enhanced chemical vapor deposition (PECVD) method.

Besides, a method to fabricate continuous and aligned multi-walled carbon nanotube/epoxy composites is also presented in this chapter. CNT/epoxy composites were made by infiltrating an epoxy resin into the aligned multi-walled CNT sheets. By controlling the alignment of the continuous multi-walled CNT sheets, a CNT/epoxy composite with high content of well-dispersed CNTs can be obtained.

2.1 Fabrication of CNT

2.1.1 Fabrication requirements

CNTs have been considered for many applications due to their unique electrical, optical, thermal and chemical properties. To meet the requirements of these applications, the CNT fabrication methods should be capable of

(a) Producing aligned CNTs since most prominent properties of CNT occur along the axis;

(b) Growing high quality nanotubes that are free of defects;

(c) Controlling the location, density, length and diameter of the CNTs.

Significant amount of research have been carried out in recent years to tackle these issues. Chemical Vapor Deposition (CVD) method has been one of promising fabrication methods due to its ability to control the synthesized carbon nanostructures.

The fabrication of the CNT using the CVD method involves heating a catalyst material on the supporting substrate to high temperature, and in a hydrocarbon gas ambient for a period of time, where the hydrocarbon source gas dissociates and precipitates on catalyst nanoparticles at high temperature. The growth temperature of high quality CNT typically takes place at high temperature ranging from 600 to 1000 ℃.

2.1.2 Substrate and catalyst preparation

Si (1 0 0) wafers are used as substrates. At the very beginning, wet station is used for cleaning the wafers. After decontamination, diffusion furnace is utilized to cover the wafer with a 100 nm thermally grown silicon dioxide. The silicon dioxide layer severed as barrier layer to prevent uncontrolled silicide formation in the subsequent process. Iron or nickel films were deposited by electron-beam evaporation method. The film thickness was monitored *in stiu* by a quartz-crystal-based thickness monitor, as well as measured *ex stiu* by an atomic force microscopy (AFM). The evaporation rate was set 0.02nm/sec at the power of 20W. The pressure in the evaporation process was 10^{-8} Torr. No substrate heating was used during the evaporation. So far, the sample has been well-prepared for loading into the PECVD system. Equipments used in the above-mentioned process are shown in Figure 2.1-1.

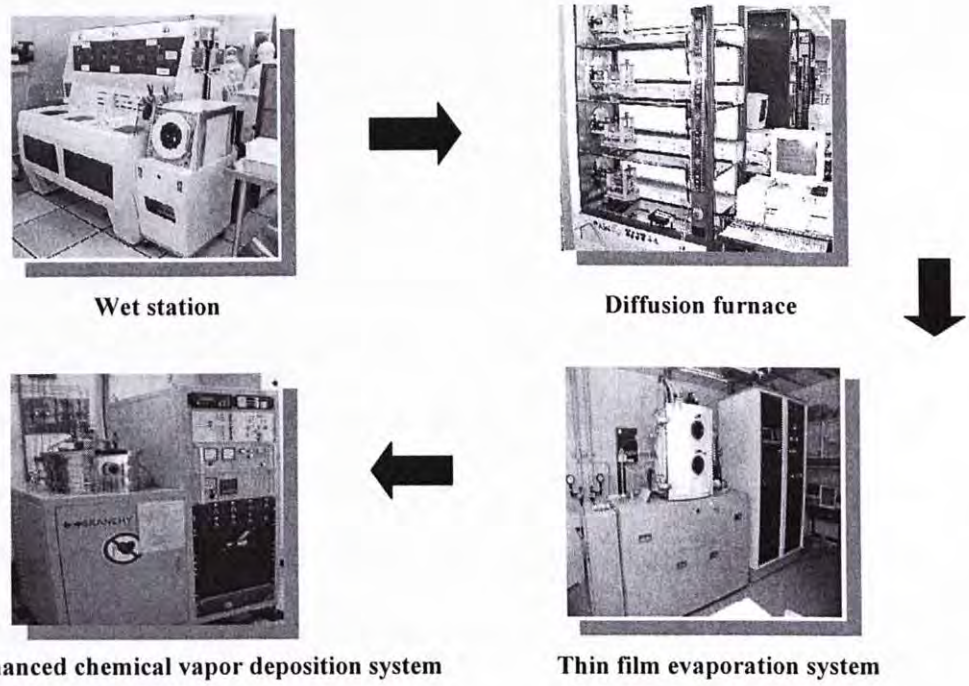

Figure 2.1-1 Equipments used in CNT fabrication processes

2.1.3 Aligned CNT film grown by PECVD method

The aligned CNT films were fabricated in an ASTEX microwave PECVD system with microwave frequency of 2.45 GHz and a maximum output power of 1500W. The substrates with the catalyst were loaded into the reactor chamber for CNT growth. The PECVD chamber was pumped to 10^{-2} Torr by mechanical pump. The hydrogen, with a flow rate of 40 sccm (standard cubic centimeter per minute), was introduced into the chamber. The RF substrate heating source was turned on, and the temperature was raised to 850℃. The hydrogen plasma was ignited and pretreated the substrate for 1 min. The substrates with catalysts were positioned at the edge of the plasma "sheath", avoiding ion bombardments. 10 sccm methane was then introduced into the reaction chamber. After a period ranging from 1 to 10 min, the microwave plasma and substrate heater were switched off to end the PECVD process. The working pressure was kept at 8 Torr. The microwave power was set at 300W. The CNT samples were examined using a JEOL 6300F scanning electron microscope (SEM) and a JEOL 2010 transmission electron microscope (TEM).

In the whole process (shown in Figure 2.1-2), the substrate plays a crucial role in CNT synthesis especially in PECVD processes. The substrate not only acts as a medium for support. It also interacts with the catalyst and growth environment. Silicon and silicon dioxide are two of the most common substrates used in CNT growth [Meyyappan et al., 2003]. Multilayered catalyst system has been developed to prevent diffusion or intermixing of catalyst and substrate [Kabir et al., 2005]. The materials are under the catalyst layer and sometimes on top of the catalyst. The significant effect of the multilayer material for CNT growth is mostly attributed to wetting and particle formation. The Al under-layer is frequently used to increase the

catalyst support surface area and decrease the probability of catalyst sintering [Cantoro et al., 2005]. Silicon dioxide layer is an excellent buffer layer to prevent the catalyst layer from diffusing and interacting with the silicon and forming a silicide. In this work, the silicon dioxide layer is also used as the supporting layer for CNT film.

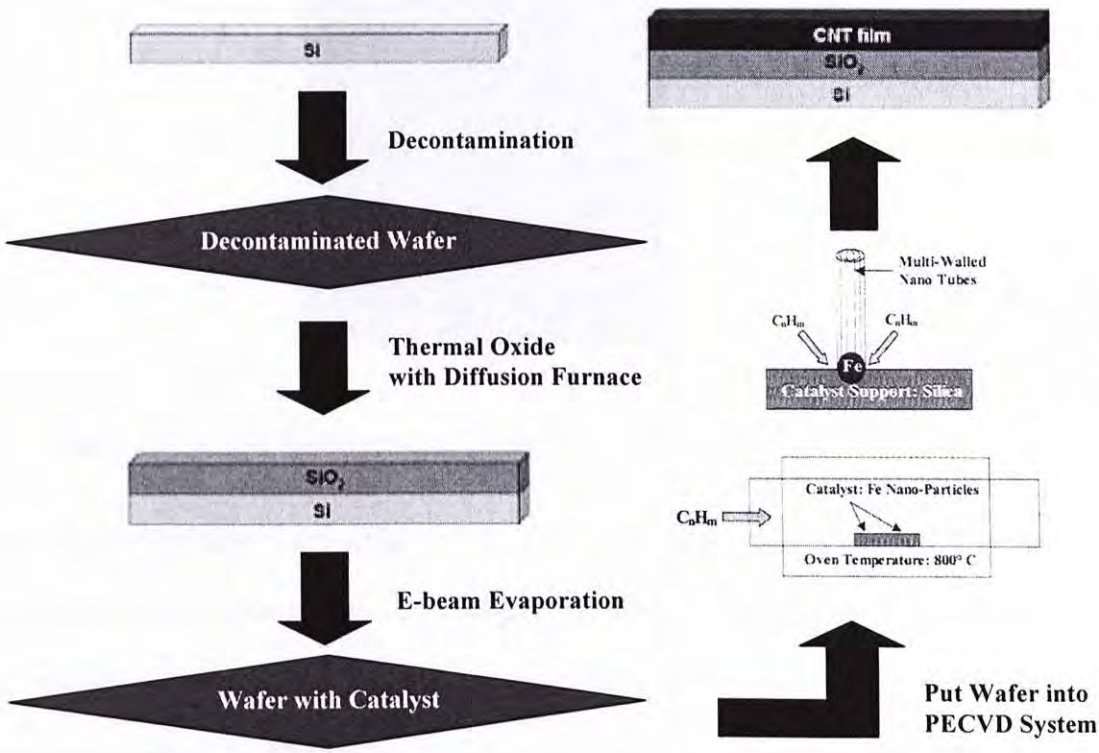

Figure 2.1-2 Process flow of fabricating carbon nanotubes

Physical vapor deposition techniques such as thermal evaporation, electron-beam evaporation and magnetron sputtering have been successfully used in catalyst preparation. The energy of the atoms evaporated by electron beam typically is on the order of tens of eV. The morphology of the thin film can be controlled by varying the power and the deposition rate during growth. However, the small grain size is not guaranteed in the as-deposited films. Hydrogen plasma ion bombardment helps to create catalyst particles with tight particle size distribution. The substrate with catalyst

is treated in the hydrogen plasma for a period of time. Figure 2.1-3 shows an AFM image of the catalyst sample after 1 min hydrogen plasma treatment. The catalyst thin film has the thickness of 5 nm used in this work. The particle size ranges from 10-15 nm.

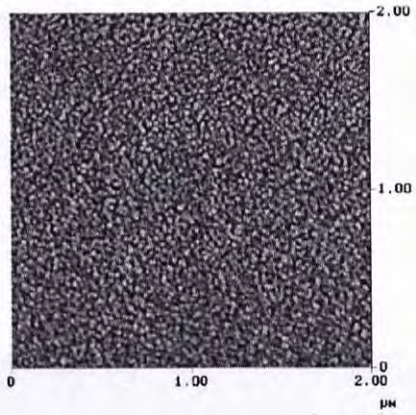

Figure 2.1-3 Atomic force microscopy image of the catalyst after plasma treatment

Ammonia and hydrogen are widely used as diluents during CNT growth. Different groups have demonstrated good CNT alignment from the gas precursor containing ammonia. However, it still remains an open question whether the nitrogen atoms will introduce impurity into the nanotube. The corrosive effect of the ammonia should be also avoided. In the case of CNT growth by PECVD, electron impact, charge exchange, ionization energy and neutral reactions should be considered. In this work, we used hydrogen and methane as gas source. Well aligned CNT film can be obtained when the ratio between hydrogen and methane is kept at 4:1.

The alignment of the dense CNT packing is believed to come from the interaction between the neighboring nanotubes, which restricts the CNT growth along other directions [Meyyappan et al., 2003]. In the case of PECVD, there are a number of report suggested that the electrical self-bias imposed on the substrate surface from the

plasma enables more vertically aligned CNTs [Zhu et al., 2000]. Figure 2.1-4 shows the as-grown CNT sample using the PECVD method. The thickness of the CNT film is determined by the growth duration and the catalyst lifetime. The site density of the aligned CNTs is about 1010 cm^{-2}. The length of the CNT in this work is 10 μm in average. Scanning Electron Microscopy characterization of the MWCNT clusters (shown in Figure 2.1-5) that decorate the surface of the silica sheets indicated the individual nanotube dimensions corresponding to ~30 nm outer diameter, ~10 nm wall thickness and the center-to-center distance between individual nanotubes in the films was determined to be approximately 50 nm.

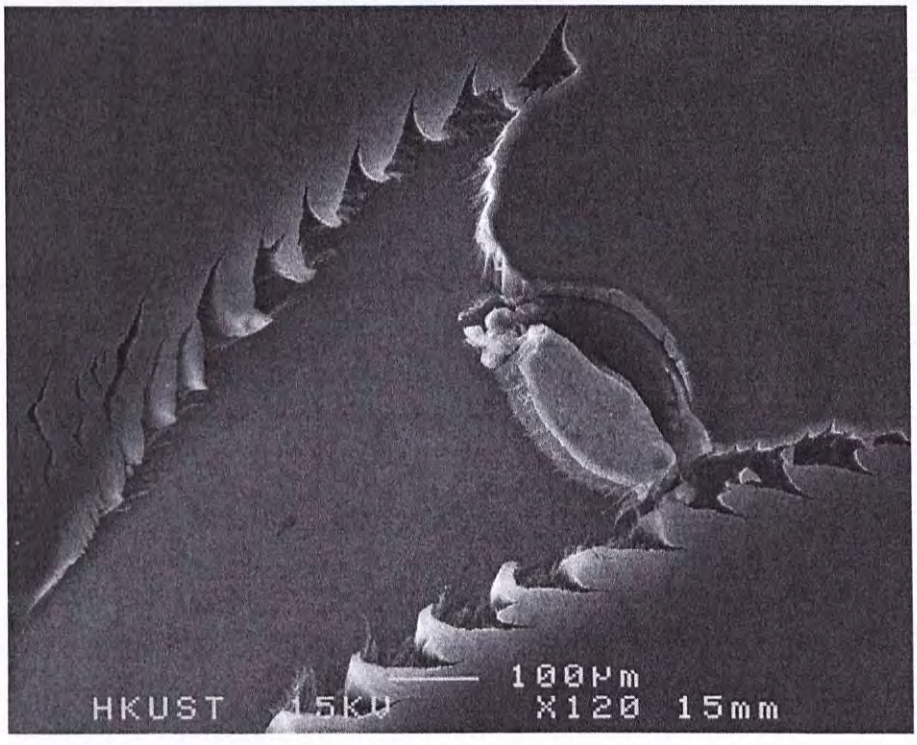

Figure 2.1-4 Overview of the as-grown CNT

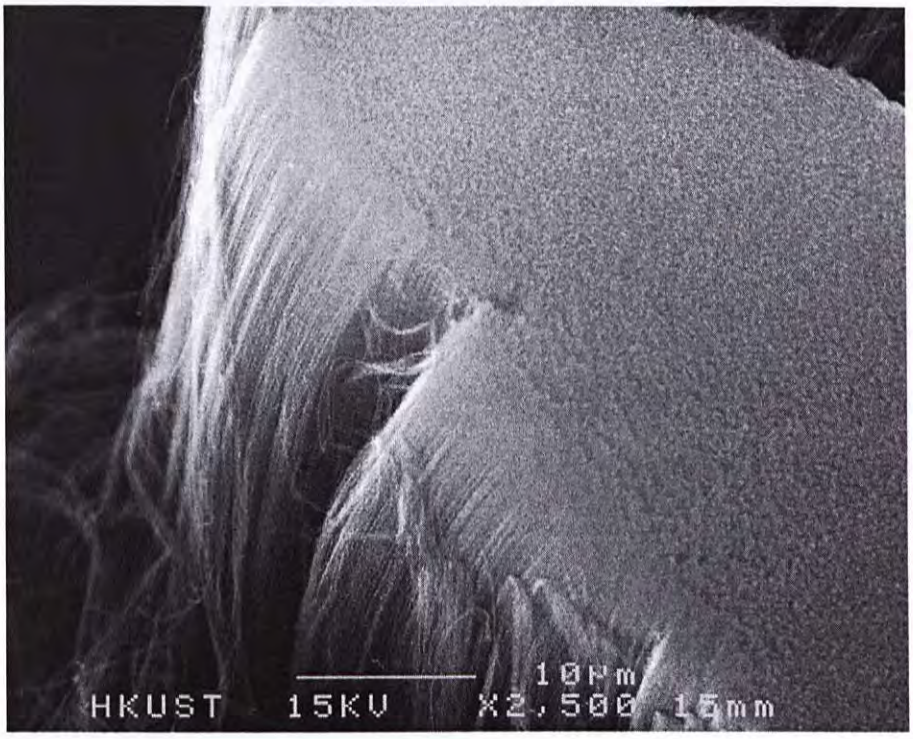

Figure 2.1-5 SEM characterization of the MWCNT clusters

The substrate surface was intentionally scratched with tweezer in order to get a clear look, so that it appears overlap in the cross-sectional area (as shown in Figure 2.1-6). Moreover, the aligned CNT arrays have very clean surfaces and it can be predicted that there are strong van der Waals forces among them.

Figure 2.1-7 is a SEM image of a continuous and aligned CNTs sheet. Figure 2.1-8 and Figure 2.1-9 are lateral faces of the as grown CNT arrays with different magnifications. Clearly, the overall alignment can be seen and the top surface is very smooth.

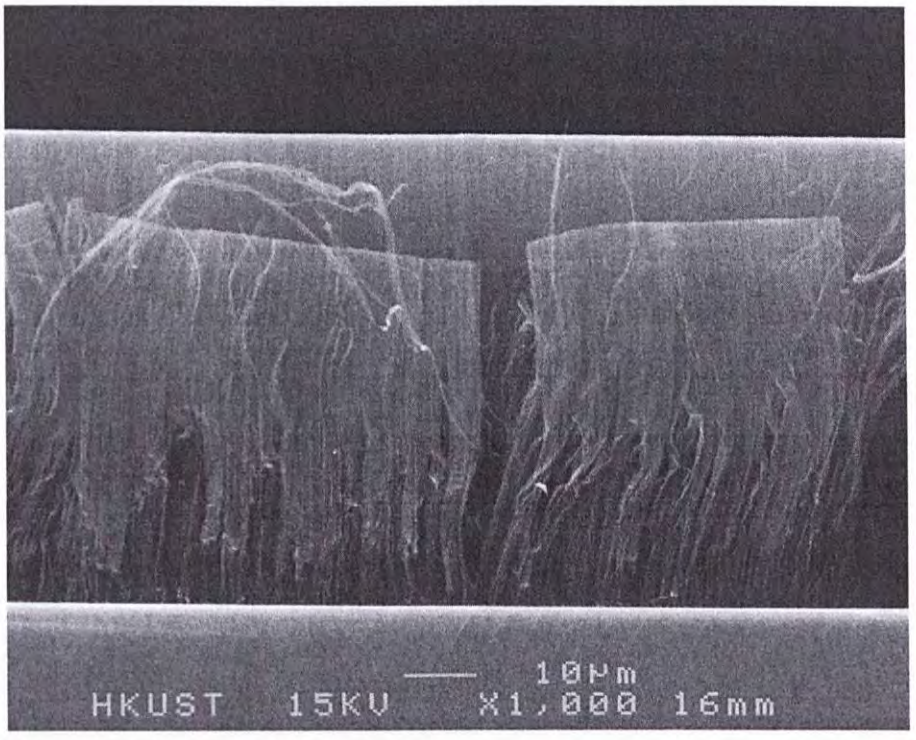

Figure 2.1-6 Cross-sectional view of the grown CNT

Figure 2.1-7 SEM image of a continuous and aligned CNT sheet

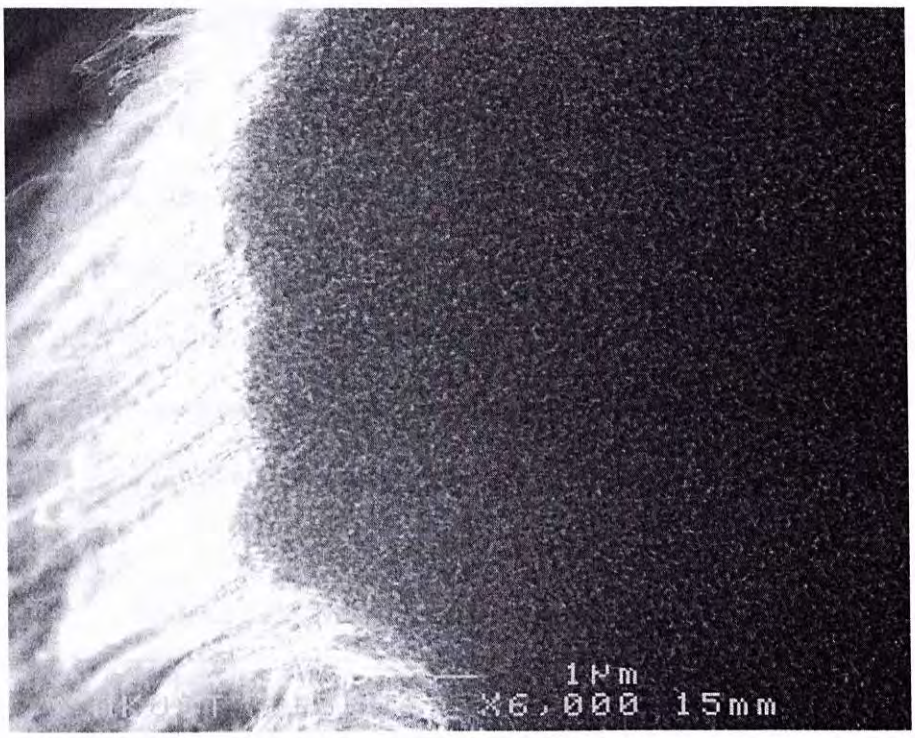

Figure 2.1-8 Lateral face of the as-grown CNT at magnification of 6000

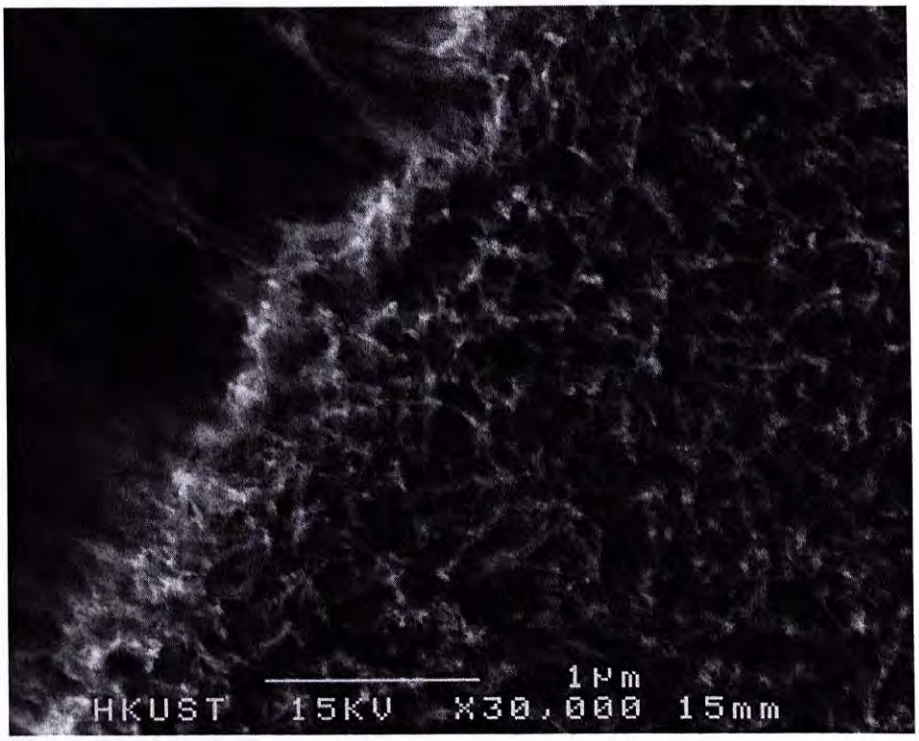

Figure 2.1-9 Lateral face of the as-grown CNT at magnification of 30000

2.2 *Fabrication of CNT/Epoxy Composite*

CNT/epoxy composites were fabricated by infiltrating an epoxy resin into the CNTs using a vacuum-assisted resin infiltration method, which requires low viscosity of the epoxy resin. In this study, an epoxy resin (Norland Optical Adhesive 84) that will cure when exposed to ultraviolet light was used. At the infiltration temperature, the viscosity of this epoxy system can be kept at as low as 15 cps for more than 12 hours. Some of the mechanical and physical properties of the epoxy are listed in Table 2.2-1.

Table 2.2-1 Physical and mechanical properties of the epoxy

Properties	Epoxy
Density (g/cm^3)	1.46
Elongation at Failure	57%
Modulus of Elasticity (GPa)	3
Poisson's ratio	0.3
Viscosity @ 25℃ (GPa・s)	15
Temperature Range	-15℃ to 90℃

The schematic of the vacuum-assisted resin infiltration process is shown in Figure 2.2-1. First, epoxy dispenser drew an epoxy perimeter on top of the CNT substrate and a piece of thin glass was coated sequentially [Figure 2.2-1 (a)]. The space between thin glass and silicon substrate can be controlled by injecting epoxy with various thicknesses. Then air in the CNT was removed in a vacuum press and the epoxy was cured to in UV lamp to form a solid state constraint [Figure 2.2-1 (b)]. The level of vacuum chamber was around 0.1 Pa to facilitate better infiltration of the epoxy resin into the CNT and to remove air bubbles in the epoxy constraint of the CNT [Figure 2.2-1 (c)]. Epoxy resin was injected into the hole to overflow and fully infiltrate the CNT by pressure difference in the atmosphere [Figure 2.2-1 (d)]. The

temperature of the oven was increased to 50℃ at a rate of 2℃/min and held at 50℃ for 25 min to cure the CNT/epoxy, forming a solid state composite [Figure 2.2-1 (e)].

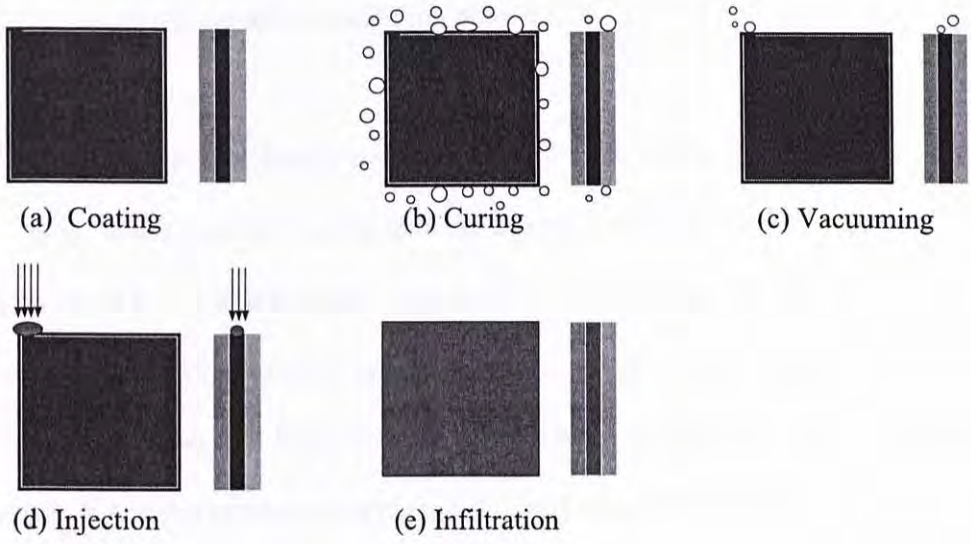

Figure 2.2-1 Schematic illustration of the CNT/epoxy composite fabrication process

(a) epoxy perimeter was drawn and coated with a thin glass; (b) air bubbles were removed in vacuum and then epoxy was cured in UV lamp (c) air bubbles in the CNT/epoxy sample were removed in vacuum; (d) epoxy resin was injected into the glass mold to infiltrate the CNTs perform; (e) CNT/epoxy composite was cured to form a solid state composite

Figure 2.2-2 shows all the equipments used during vacuum-assisted resin infiltration process. Epoxy dispenser is an apparatus for dispensing adhesives with premeasured adhesive portions contained in compartments of a package. It facilitates the application of epoxies that are subject to changes in viscosity and can provide precise, repeatable results, despite changes in fluid volume, viscosity and temperature. The compact dispenser is electromechanically operated, with no air pressure required and is compatible with the syringe barrels and dispensing tips.

Vacuum press consists of nothing more than a vinyl bag with a pump attached to evacuate the air from the bag. The press relies on atmospheric pressure to press the veneer against the substrate while it is being glued. Additionally, vacuum presses produce a surprising amount of clamping pressure.

UV lamp is a lamp specifically designed to emit light at the ultraviolet wavelength, which is generally not able to be seen by humans without special equipment. The epoxy is cured by ultraviolet light with maximum absorption within the range of 320-400 nanometers. After curing, the epoxy turns to be a solid state. In the whole experimental process, UV lamp needs to be used twice. Firstly it is used to cure epoxy perimeter. When the perimeter becomes solid, it is also turns to be a constraint, which is able to avoid internal fluid moving out. Then after fully filling the internal regions with epoxy, UV lamp will be used again to cure the CNT/epoxy composite.

Vacuum chamber is designed and built to remove air and moisture from the sample while its surrounding is under vacuum and then inject a drop of epoxy manually at the gap of the perimeter with a small tube while also under vacuum. Then the pressure inside the vacuum chamber should be increased gradually until reaching the atmosphere. That drop of epoxy was injected into the perimeter to overflow and fully infiltrate the CNT by pressure difference between inside vacuum and outside atmosphere.

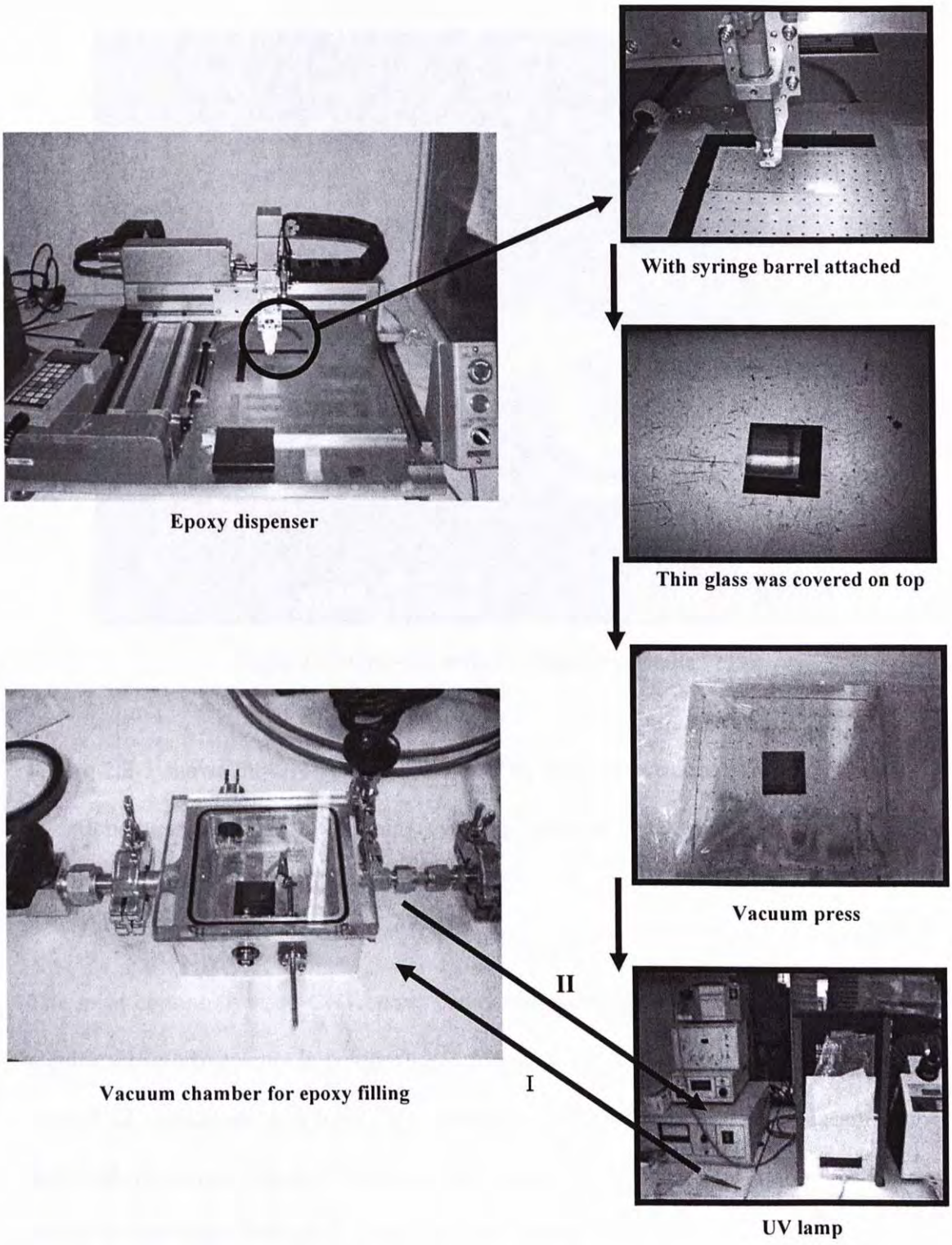

Figure 2.2-2 Equipments used during vacuum-assisted resin infiltration process

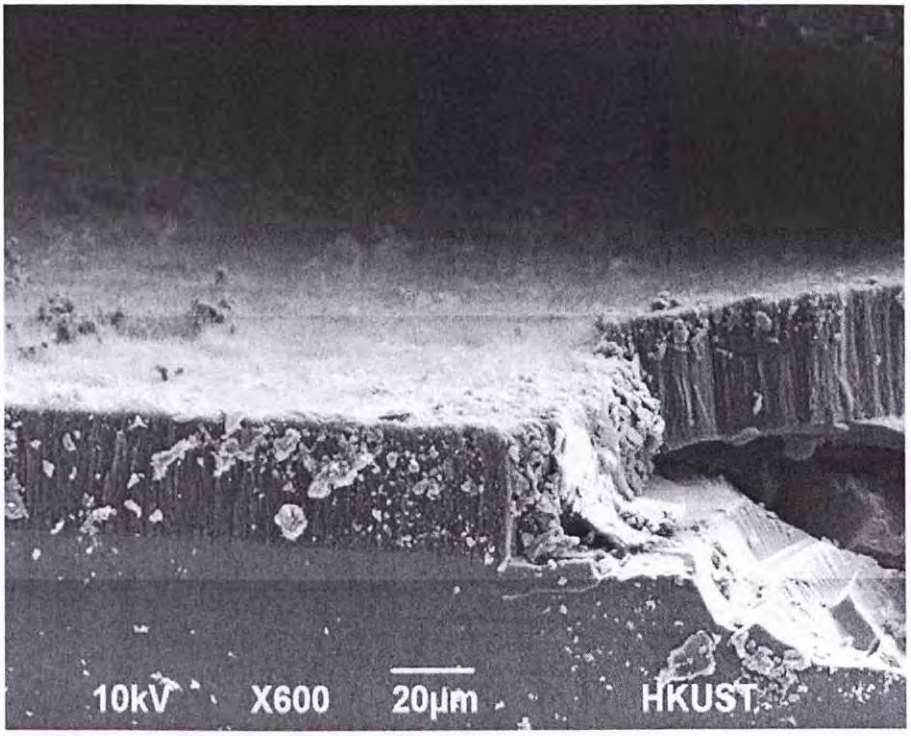

Figure 2.2-3 Overview of the CNT/epoxy composite

Figure 2.2-3 shows the CNT/epoxy composite by SEM observation. The sample was intentionally cut through by hobbing cutter in order to check the inner area. As a result, it appears irregularity on partial surfaces.

The most commonly used CNT/epoxy composites fabrication methods can not yield significant improvements in composite performance because effective dispersion and controlled orientation of a high CNT content in the epoxy resin matrix can not be achieved. However, Figure 2.2-4 proves the vacuum-assisted resin infiltration method is able to fabricate CNT/epoxy composites by infiltrating epoxy resins into a stack of continuous and aligned multiwalled CNT sheets to achieve homogeneous dispersion, controlled orientation, and high CNT content.

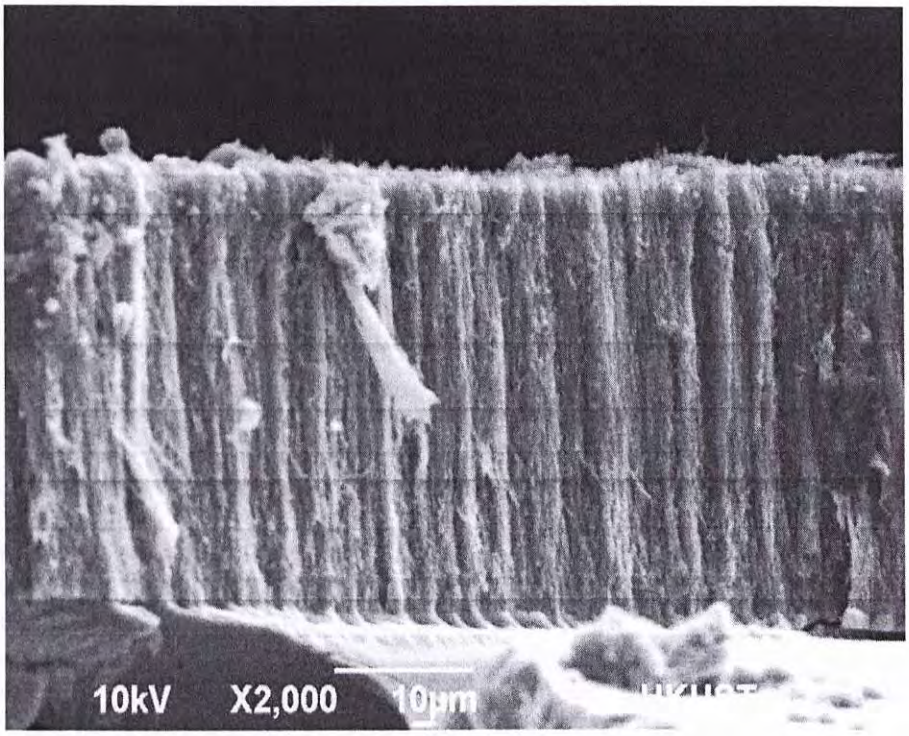

Figure 2.2-4 Cross section of the CNT/epoxy composite with magnification of 2000

2.3 Measurement of CNT/Epoxy Composites

CNT/epoxy composites were fabricated by infiltrating epoxy resin into the CNTs using a vacuum-assisted resin infiltration method. However, since the sample is very small, it is hard to tell whether the epoxy has been impregnated in the CNTs or only suspended on top of CNTs. To verify if the epoxy has been impregnated in the CNT layer, analysis is necessary to be performed.

Fourier transform infra-red (FTIR) spectroscopy is a measurement technique for collecting infrared spectra. Instead of recording the amount of energy absorbed when the frequency of the infra-red light is varied, the IR light is guided through an interferometer. After passing through the sample, the measured signal is the interferogram. Performing a mathematical Fourier transform on this signal results in a spectrum identical to that from conventional infrared spectroscopy.

For the purpose of confirming the epoxy impregnated into the CNT layer, FTIR analysis was performed in Attenuated Total Reflectance (ATR) mode on 4 samples, which are A (a layer of epoxy in CNTs removed from B), B (Epoxy in CNTs), C (Pure Epoxy), and D (Pure CNTs).

For A, a layer of epoxy was scratched off with paper knife in order to assure epoxy being present in the CNT layer (Inside the CNT region); For B, the sample was kept intact and performed FTIR analysis on the surface (surface region of the CNTs); For C, the pure epoxy is a reference to compare the FTIR spectra collected from A and B; For D, the pure CNTs is another reference from which the information can be

collected whether or not the pure CNTs will give significant FTIR to interfere the result.

Referring to the overlay spectra in the result [Figure 2.3-1], it can be seen that spectra A and B look identical to C. From this comparison, it can be summarized that epoxy material is found in A (inside the CNTs) and B (surface region).

On the other hand, all the tests were conducted on the basis of removal of thin glass layer. The total thickness of the testing sample is 44.7 μm, and the thickness of CNT/epoxy composite is about 20 μm. Detected by Alpha-Step 500, the thickness of the polished layer is 39 μm. For polishing 39 μm, the measured point is inside the CNT region [Figure 2.3-2].

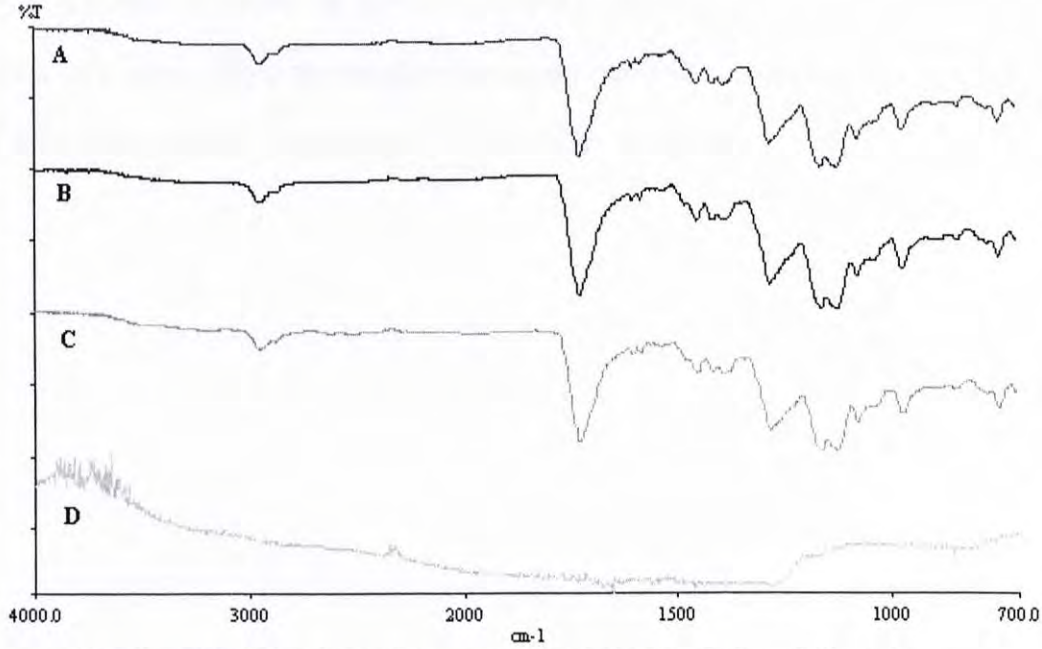

A: Epoxy/CNT with removal of the uppermost layer (polished 39 μm thickness)
B: Epoxy/CNT without removal of the uppermost layer
C: Epoxy
D: CNT

Figure 2.3-1 FTIR analysis results for four samples

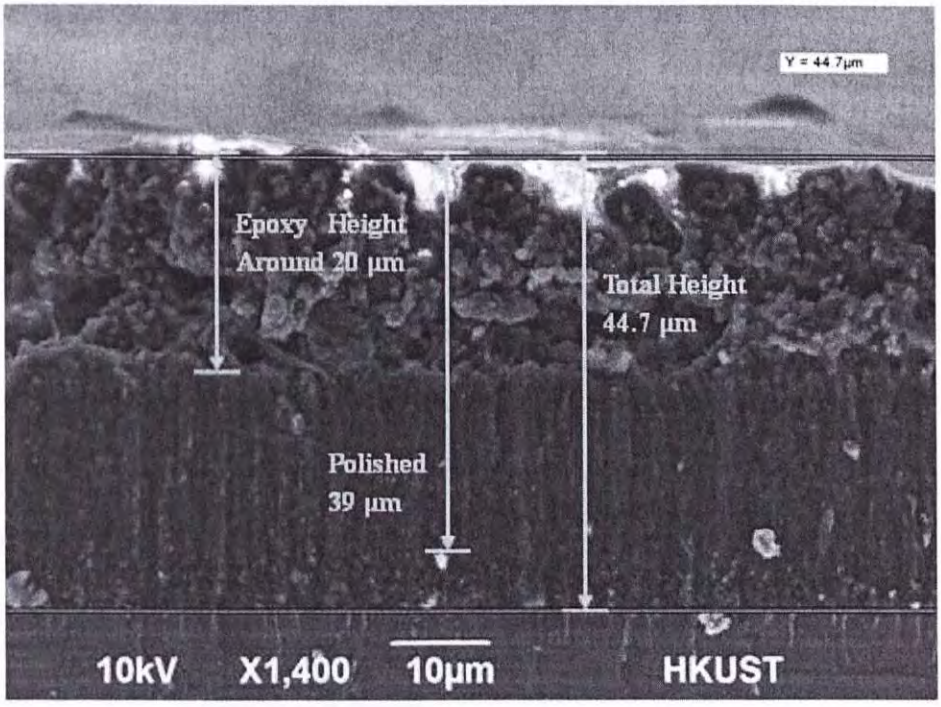

Figure 2.3-2 Measured CNT/epoxy sample with marked height

The thickness of epoxy on top of CNT/epoxy composite can be controlled by the epoxy dispenser. When the height of the epoxy perimeter is the same as the length of CNTs, the top epoxy layer will be gone, as shown in Figure 2.2-4.

2.4 Chapter Summary

Fabrication procedures for high density aligned multi-walled CNTs and the CNT/epoxy composite are given in this chapter. The individual nanotube dimensions as well as the center-to-center distance next to each other can be observed by scanning electron microscopy, which will be useful for structural modeling. The observing results also show that the vacuum-assisted resin infiltration method is able to fabricate CNT/epoxy composites by infiltrating epoxy resins into a stack of aligned multiwalled CNT sheets to achieve homogeneous dispersion, controlled orientation, and high CNT content, while none of previous experiments achieved.

CHAPTER THREE

MODELLING OF THE CNT COMPOSITES

It was predicted that the CNT addition gives the composite significant damping enhancement. It is important and interesting to find out what causes this energy dissipation, what the mechanism is and how to optimize the damping effect.

Computational models allow us to obtain material characteristics even before making the composite. It is helpful to predict mechanical properties such as stiffness and damping of the composite and provide us with a reasonable scope to our anticipation. Thus, computational models play an important role in the CNT composite research.

In this chapter, high density aligned multi-walled carbon nanotube is modeled. The resin is described as a viscoelastic material using Maxwell model and three-parameter standard solid model, respectively. The CNT/epoxy composite is modeled based on the "stick-slip" mechanism, to describe the load transfer behavior between the CNT and its sheath. In order to further study the damping mechanism of the CNT composite, key parameters that are expected to affect the composite damping performances are studied.

3.1 Geometrical Configuration of Composites

The CNT will be modeled using a hollow continuous cylinder with a length l_{nt} and an outer radius R_{nt}. The wall thickness t_{nt} can be detected by Scanning Electron Microscopy (SEM). The Young's and shear moduli of graphite sheet, denoted E_g and G_g, are assumed to apply to the CNTs. To simplify the model without losing accuracy, the CNTs are replaced by solid cylinders with the same length and outer radius of the nanotube, and Young's and shear moduli are adjusted based on the equivalence of extensional and torsion stiffness. Letting α denote t_{nt}/R_{nt}, the elastic properties of the solid cylinder are obtained as follows:

$$E_{eq} = 2\alpha E_g \tag{3.1}$$

$$G_{eq} = (1-(1-\alpha)^4)G_g \tag{3.2}$$

For vertically aligned multi-walled CNT, each CNT segment is assumed to have the same dimension, orientation and center-to-center distance (Figure 3.1-1). The epoxy resin fully fills the space among individual CNT segments, implying that no interactions exist between CNTs. Therefore, only one type of load transfer will be considered in the composite: the interactions at the CNT/sheath interfaces. For each CNT, the contact area with the sheath is its whole circumferential area.

Furthermore, the nanotube is assumed to be surrounded by a sheath of resin in a unit cell of the composite. The sheath carries all the shear stress between nanotubes and the remote resin material. Since the volume fraction of the sheath is very small compared to the resin, its z-direction normal stress is assumed to be negligible. The

CNT axis is situated parallel to the applied stress direction. Both thickness and width of the unit cell are $d+2R_{nt}$, which are related with the dimension of CNT segment. And the length is equal to the length of CNT segment, l_{nt} (Figure 3.1-2).

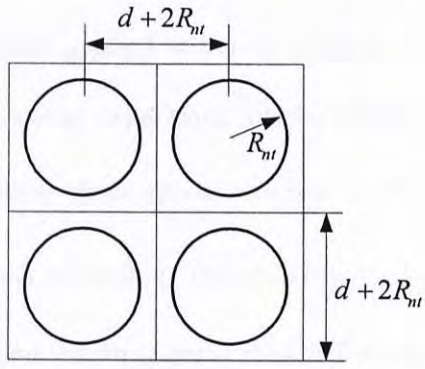

Figure 3.1-1 Top-view schematic of CNT/epoxy composite

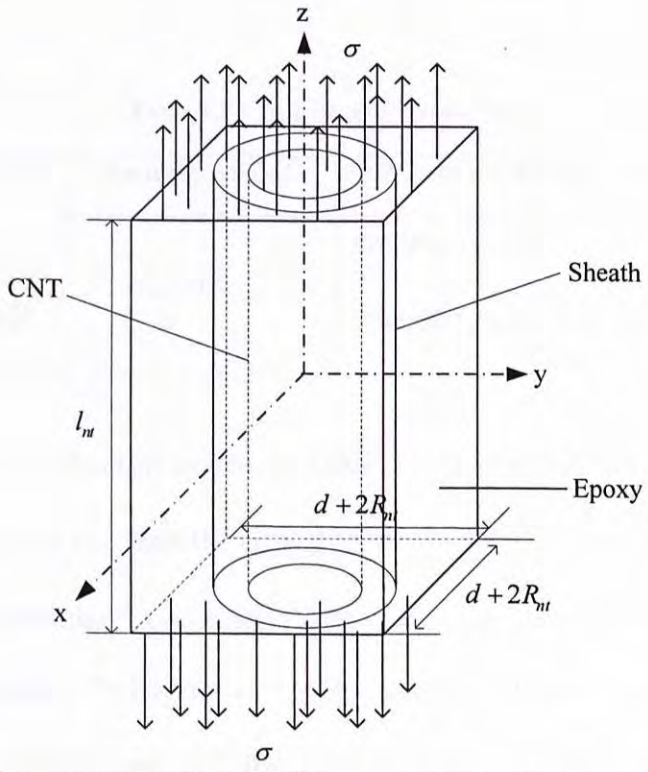

Figure 3.1-2 Unit cell consisting of a CNT surrounded by a sheath and remote resin

3.2 Critical Shear Stresses and "Stick-Slip" Behavior

Consider an initially perfectly bonded composite consisting of a resin and a CNT surrounded by a sheath. Due to the high aspect ratio of CNT, load transfer at the ends of CNTs is neglected. As the applied stress is a harmonic loading and increases monotonically, some CNTs could experience interfacial debonding. In this research, τ_{nt}^{c} is defined to be the critical shear stress between CNT and the sheath, which is used to characterize the onset of sliding. The quantity τ_{nt}^{c} represents the shear stress required between the CNT and sheath to break the CNT/sheath bond. The CNT/sheath interactions involve the functional bonds between CNT and the specific monomer structures of the polymer.

Table 3.2-1 Deformation development

Shear stress on CNT	**Perfectly bonded**	**CNT/sheath sliding**	**After fully debonded**
$\tau_{nt}(z)$ $z \in (-l_{nt}/2, l_{nt}/2)$	$\tau_{nt}(z) \le \tau_{nt}^{c}$	**Partially** $\tau_{nt}(z) = \tau_{nt}^{c}$ **Overall** $\tilde{\tau}_{nt}(z) \le \tau_{nt}^{c}$	$\tilde{\tau}_{nt}(z) = \tau_{nt}^{c}$

The "stick-slip" mechanism (given in Table 3.2-1) provides that, if the interfacial shear stress $\tau_{nt}(z)$ is less than the critical value τ_{nt}^{c}, the CNT and sheath will sustain an identical deformation. As the applied load increases, the debonded proportion of the interface between CNT and sheath will gradually increase. The strain value of the CNT in the debonded part will not increase since the shear stress at debonded interface remains constant. Debonding starts at the end of the nanotube and is assumed to gradually extend to the full length of the nanotube. During this debonding process, the CNT and the sheath have different elongations, leading to a slippage

between them. The length change of the CNT is l_{nt} when the debonding between the CNT and the sheath is fully developed.

3.3 Nonlinear Viscoelastic Composite Model

Since the aspect ratio of the nanotube is very large and the "stick-slip" motion is only considered in the longitudinal direction of the nanotube, the CNT-based composite is modeled as a viscoelastic element and a Coulomb friction element in parallel. The Coulomb friction element represents nonlinear response due to the "stick-slip" movement. Based on the viscoelasticity theory [Shames et al., 1991], two viscoelastic models are applied in this nonlinear model: Maxwell model and three-parameter standard solid model.

3.3.1 Maxwell model

The Maxwell model can be represented by a purely viscous damper and a purely elastic spring connected in series (Figure 3.3-1).

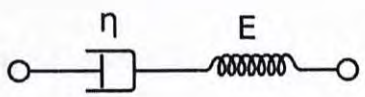

Figure 3.3-1 Maxwell model

Under an applied axial stress, the total stress and total strain can be defined as:

$$\begin{aligned} \sigma &= \sigma_D = \sigma_S \\ \varepsilon &= \varepsilon_D + \varepsilon_S \end{aligned} \tag{3.3}$$

where the subscript D indicates the stress/strain in the damper and the subscript S indicates the stress/strain in the spring. Taking the derivative of strain with respect to time,

$$\frac{d\varepsilon}{dt} = \frac{d\varepsilon_D}{dt} + \frac{d\varepsilon_S}{dt} = \frac{\sigma}{\eta} + \frac{1}{E}\frac{d\sigma}{dt} \tag{3.4}$$

where E is the elastic modulus and η is the material coefficient of viscosity. The total strain rate is composed of two parts. The spring element in the model responds by contributing a strain rate directly proportional to and in phase with the spring stress rate. However, the damper strain rate responds only to the instantaneous level of damper stress.

In order to formulate differential equations governing the behavior of materials represented by Maxwell model, operator D is used for the derivative $\partial/\partial t$. Using operator D, equation (3.4) can be expressed as:

$$D\varepsilon = \frac{\sigma}{\eta} + \frac{D\sigma}{E} \tag{3.5}$$

Equation (3.5) can be rewritten as:

$$\varepsilon = \frac{\sigma}{D\eta} + \frac{\sigma}{E} \tag{3.6}$$

Next find the common denominator for the right side of the equation,

$$D\eta E\varepsilon = E\sigma + D\eta\sigma \tag{3.7}$$

Using dots to represent the operator D, equation (3.7) can be rewritten as:

$$\eta E\dot{\varepsilon} = E\sigma + \eta\dot{\sigma} \tag{3.8}$$

Now for Maxwell model, there arrives at a linear differential equation, which can be expressed compactly as:

$$P^E\sigma = Q^E\varepsilon \tag{3.9}$$

Here the subscript E refers to Young's modulus, P^E and Q^E are linear differential operators given by

$$\begin{aligned} P^E &= \sum_{i=0}^{m^E} p_i{}^E \frac{\partial^i}{\partial t^i} = p_i{}^E D^i \\ Q^E &= \sum_{i=0}^{n^E} q_i{}^E \frac{\partial^i}{\partial t^i} = q_i{}^E D^i \end{aligned} \tag{3.10}$$

where p^E's and q^E's are to be considered as constants under isothermal conditions. Set $p_0{}^E = 1$ to normalize the differential equation by dividing through by the coefficient of the zeroth-order derivative of σ. This procedure is always possible

since for spring-damper models the coefficient of the zeroth-order derivative of stress is never zero. For the Maxwell model, we can rewrite equation (3.8) as

$$q_1^E \dot{\varepsilon} = \sigma + p_1^E \dot{\sigma} \tag{3.11}$$

Here $q_0^E = 0, q_1^E = \eta, p_1^E = \frac{\eta}{E}$, so that $P^E = 1 + \frac{\eta D}{E}, Q^E = \eta D$. Now an analogy between the tensile test formulation for the elastic case and the viscoelastic case has been established. The tensile operator ratio for the axial direction is

$$Q^E / P^E \sim E \tag{3.12}$$

In a manner similar to the tensile test, for the viscoelastic case,

$$P^G \tau_{xy} = Q^G \varepsilon_{xy} \tag{3.13}$$

Here P^G, Q^G are linear operator pairs for shear. By isotropic Hooke's law,

$$\gamma_{xy} = 2\varepsilon_{xy} = \frac{1}{G}\tau_{xy} \tag{3.14}$$

The shear operator ratio can be obtained as

$$Q^G / P^G \sim 2G \tag{3.15}$$

where G is the shear modulus of elasticity. The operators P^G and Q^G are given by the same formulations as in equation (3.10) but with superscript G. In addition to the tensile test and shear test, pressure test should also be considered.

$$P^K \bar{\tau} = Q^K \bar{\varepsilon} \tag{3.16}$$

For the viscoelastic material, P^K and Q^K are another operator pairs, where K is the bulk modulus. Based on the relations between elastic constants in isotropic Hooke's Law, one more analogy relation is the pressure operator ratio:

$$Q^K / P^K \sim 3K \tag{3.17}$$

The forms of Q^K and P^K are again given in equation (3.10) but now with the superscript K. Now the analogy between linear elastic materials and viscoelastic materials can be described as follows:

$$\begin{bmatrix} \bar{E}(t) \\ \bar{G}(t) \\ \bar{K}(t) \end{bmatrix} = \begin{bmatrix} Q^E / P^E \\ Q^G / P^G \\ Q^K / P^K \end{bmatrix} \sim \begin{bmatrix} E \\ 2G \\ 3K \end{bmatrix} \tag{3.18}$$

The parameters with an overbar are used to denote viscoelastic material properties. From the relations between elastic constants for isotropic forms of Hooke's law, the shear modulus G is expressed in terms of the Young's modulus and the bulk modulus by

$$G = \frac{3EK}{9K - E} \tag{3.19}$$

Similarly the Poisson's ratio ν can be expressed in terms of the Young's modulus and the bulk modulus by

$$\nu = \frac{3K - E}{6K} \tag{3.20}$$

As a result, the shear modulus of the Maxwell model is as follows:

$$\begin{aligned} \bar{G}(t) &= \frac{3\bar{E}(t)\frac{\bar{K}(t)}{3}}{9\frac{\bar{K}(t)}{3} - \bar{E}(t)} = \frac{(\frac{Q^E}{P^E})(\frac{Q^K}{P^K})}{3(\frac{Q^K}{P^K}) - \frac{Q^E}{P^E}} = \frac{\frac{\eta D}{1+(\eta/E)D} \cdot 3K}{3 \cdot 3K - \frac{\eta D}{1+(\eta/E)D}} \\ &= \frac{3\eta KED}{9KE + 9K\eta D - E\eta D} \end{aligned} \tag{3.21}$$

$$\begin{aligned} \bar{\nu}(t) &= \frac{3\frac{\bar{K}(t)}{3} - \bar{E}(t)}{6\frac{\bar{K}(t)}{3}} = \frac{\frac{Q^K}{P^K} - \frac{Q^E}{P^E}}{2\frac{Q^K}{P^K}} = \frac{3K - \frac{\eta D}{1+\frac{\eta D}{E}}}{2 \cdot 3K} \\ &= \frac{3EK + 3\eta KD - E\eta D}{6KE + 6K\eta D} \end{aligned} \tag{3.22}$$

3.3.2 Three-parameter standard solid model

Materials undergoing strain are often modeled with mechanical components, such as spring (restorative force component) and dashpots (damping component). Connecting a spring and damper in series yields a model of a Maxwell material while standard

solid model is slightly more complex, involving elements both in series and in parallel (Figure 3.3-2).

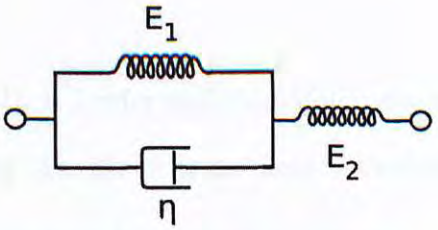

Figure 3.3-2 Three-parameter standard solid model

Springs, which represent the elastic component of a viscoelastic material, obey Hooke's law:

$$\sigma_s = E\varepsilon \tag{3.23}$$

Dashpots represent the viscous component of a viscoelastic material. In the dashpot element, the applied stress varies with the time rate of change of the strain:

$$\sigma_D = \eta \frac{d\varepsilon}{dt} \tag{3.24}$$

The standard solid model consists of two systems in series. The first, referred to as the Kelvin-Voigt arm, contain a spring ($E = E_1$) and dashpot (viscosity η) in parallel. The other system contains only a spring ($E = E_2$). In order to model the whole system, the following relationships help to relate the various stresses and strains in the overall system:

$$\begin{aligned}\sigma &= \sigma_K = \sigma_2 \\ \varepsilon &= \varepsilon_K + \varepsilon_2 \\ \sigma_K &= \sigma_D + \sigma_1 \\ \varepsilon_K &= \varepsilon_D = \varepsilon_1\end{aligned} \tag{3.25}$$

where the subscripts *K, D*, 1, 2 refer to Kelvin-Voigt, dashpot, spring one and spring two, respectively. Using the above stress-strain relationships for the spring and dashpot elements, the system can be modeled as follows:

$$\sigma = \eta\dot{\varepsilon}_1 + E_1\varepsilon_1 = E_2\varepsilon_2 \tag{3.26}$$

$$\varepsilon = \varepsilon_1 + \varepsilon_2 \tag{3.27}$$

Using the differentiate operator *D*, the above relationship may be expressed as:

$$\varepsilon = \frac{\sigma}{E_1 + \eta D} + \frac{\sigma}{E_2} \tag{3.28}$$

Next find the common denominator for the right side of the equation and multiply ε by this expression:

$$E_2(E_1 + \eta D)\varepsilon = E_2\sigma + (E_1 + \eta D)\sigma \tag{3.29}$$

Using dots to represent the operator *D*,

$$E_2E_1\varepsilon + \eta E_2\dot{\varepsilon} = (E_2 + E_1)\sigma + \eta\dot{\sigma} \tag{3.30}$$

Again there arrives at a linear differential equation. This equation can be expressed compactly as:

$$P\sigma = Q\varepsilon \tag{3.31}$$

Here P and Q are linear differential operators given by

$$\begin{aligned} P &= \sum_{i=0}^{m} p_i \frac{\partial^i}{\partial t^i} = p_i D^i \\ Q &= \sum_{i=0}^{n} q_i \frac{\partial^i}{\partial t^i} = q_i D^i \end{aligned} \tag{3.32}$$

where p's and q's are to be considered as constants under isothermal conditions. Set $p_0 = 1$ to normalize the differential equation by dividing through by the coefficient of the zeroth-order derivative of σ. For the standard solid model, we can rewrite equation (3.30) as

$$q_0\varepsilon + q_1\dot{\varepsilon} = \sigma + p_1\dot{\sigma} \tag{3.33}$$

Here $q_0 = \frac{E_1E_2}{E_1+E_2}$, $q_1 = \frac{E_1\eta}{E_1+E_2}$, $p_0 = 1$, $p_1 = \frac{\eta}{E_1+E_2}$, so that

$$P = 1 + \frac{\eta D}{E_1+E_2}, \quad Q = \frac{E_1(E_2+\eta D)}{E_1+E_2} \tag{3.34}$$

From equations (3.13-3.20), the shear modulus and Poisson's ratio of the standard solid model are derived as follows:

$$\bar{G}(t)=\frac{3\bar{E}(t)\frac{\bar{K}(t)}{3}}{9\frac{\bar{K}(t)}{3}-\bar{E}(t)}=\frac{(\frac{Q^E}{P^E})(\frac{Q^K}{P^K})}{3(\frac{Q^K}{P^K})-\frac{Q^E}{P^E}}=\frac{\frac{E_1(E_2+\eta D)}{E_1+E_2+\eta D}\cdot 3K}{3\cdot 3K-\frac{E_1(E_2+\eta D)}{E_1+E_2+\eta D}} \qquad (3.35)$$

$$=\frac{3E_1K(E_2+\eta D)}{9K(E_1+E_2+\eta D)-E_1(E_2+\eta D)}$$

$$\bar{\nu}(t)=\frac{3\frac{\bar{K}(t)}{3}-\bar{E}(t)}{6\frac{\bar{K}(t)}{3}}=\frac{\frac{Q^K}{P^K}-\frac{Q^E}{P^E}}{2\frac{Q^K}{P^K}}=\frac{3K-\frac{E_1(E_2+\eta D)}{E_1+E_2+\eta D}}{2\cdot 3K} \qquad (3.36)$$

$$=\frac{1}{2}-\frac{E_1(E_2+\eta D)}{6K(E_1+E_2+\eta D)}$$

3.4 Stress and Strain Evaluation

A shear lag analysis is used to characterize load transfer around a CNT. The normal stress and shear stress acting on the outside of CNT in the z-direction are represented by $\sigma_{nt}(z)$ and $\tau_{nt}(z)$, respectively. With the assumption that the normal stress in the resin is spatially uniform and that the normal stress in the sheath is negligible, the overall equilibrium along z-direction of the unit cell (Figure 3.4-1) gives

$$\pi R_{nt}^2 \cdot \sigma_{nt}(z) + [(d+2R_{nt})^2 - \pi R_{sh}^2] \cdot \sigma_{rs} = \sigma \cdot (d+2R_{nt})^2 \tag{3.37}$$

where R_{sh} is the outer radius of the sheath, σ is the normal stress applied on the composite in the z-direction, and σ_{rs} is the normal stress in the resin along the z-direction.

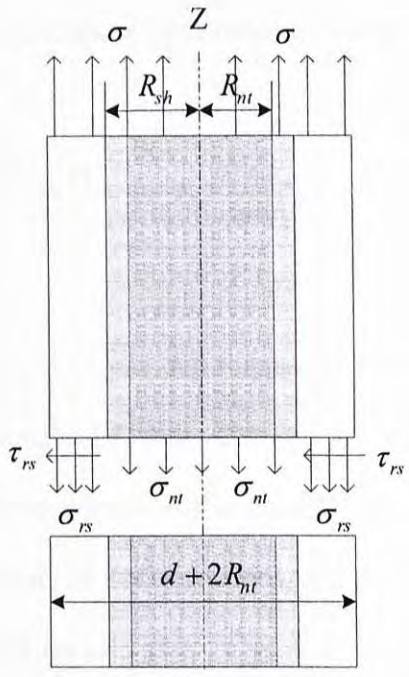

Figure 3.4-1 Stresses in unit cell when subjecting external normal stress

The shear strain in the sheath γ_{sh} is determined from the displacement of the CNT (u_{nt}) and the resin (u_{rs}) along the z-direction:

$$u_{rs} - u_{nt}(z) = (R_{sh} - R_{nt}) \cdot \gamma_{sh}(z) \tag{3.38}$$

Taking the first derivative of equation (3.38) with respect to z and using the strain-displacement and stress-strain relations,

$$\varepsilon_{rs} - \varepsilon_{nt}(z) = \frac{\sigma_{rs}}{E_{rs}} - \frac{\sigma_{nt}(z)}{E_{eq}} = \frac{R_{sh} - R_{nt}}{G_{rs}} \cdot \frac{d\tau_{nt}(z)}{dz} \tag{3.39}$$

where E_{rs} and G_{rs} are the Young's modulus and shear modulus of the resin, ε_{rs} and $\varepsilon_{nt}(z)$ are the normal strains of the resin and CNT in the z-direction, respectively. As shown in Figure 3.4-2, the applied stress is assumed to be transferred to the CNT through a CNT-resin interfacial shear mechanism as follows:

$$\frac{d\sigma_{nt}(z)}{dz} = -\tau_{nt}(z) \cdot \frac{2\pi R_{nt}}{\pi R_{nt}^2} = -\frac{2\tau_{nt}(z)}{R_{nt}} \tag{3.40}$$

Based on the "stick-slip" concept, the deformation of a CNT can be described as: at the very beginning, no interfacial debonding occurs anywhere in the composite system. Therefore, there is no energy loss at the CNT/sheath interfaces. In this case, the normal stresses at the ends of CNTs are zero, and the shear stresses at the middle lengths of the CNTs (z = 0) are also zero. In general, the boundary conditions for all the CNTs are

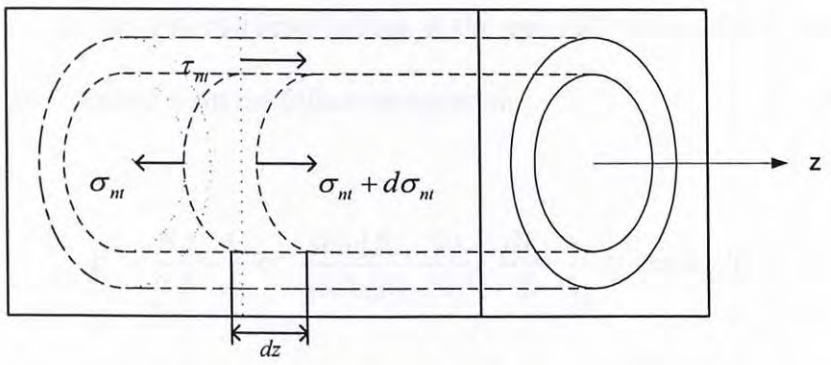

Figure 3.4-2 Schematic of stresses on a nanotube in resin

$$\sigma_{nt}(z=\pm l_{nt}/2)=0;\ \tau_{nt}(z=0)=0 \tag{3.41}$$

By substituting equations (3.37), (3.40) into equation (3.39), and utilizing the boundary conditions (equation (3.41)), the stress distributions are given by

$$\sigma_{nt}(z)=\frac{k_3}{k_2}\sigma[1-\frac{\cosh(\beta z)}{\cosh(\beta l_{nt}/2)}] \tag{3.42}$$

$$\tau_{nt}(z)=\frac{\beta R_{nt}}{2}\frac{k_3}{k_2}\sigma\cdot\frac{\sinh(\beta z)}{\cosh(\beta l_{nt}/2)} \tag{3.43}$$

where $\beta^2=\frac{k_2}{k_1\lambda}$, $\lambda=(d+2R_{nt})^2$, k_1,k_2,k_3 are non-dimensional coefficients defined by

$$k_1=\frac{E_{rs}}{2G_{rs}}\frac{(R_{sh}-R_{nt})R_{nt}}{\lambda};\ k_2=\frac{\pi R_{nt}^2}{\lambda}k_3+\frac{E_{rs}}{E_{eq}};\ k_3=\frac{\lambda}{\lambda-\pi R_{sh}^2} \tag{3.44}$$

According to equation (3.43), frictional sliding of the CNT occurs when the magnitude of $\tau_{nt}(z=\pm l_{nt}/2)$ equals to the critical value τ_{nt}^c. At this point in loading,

the corresponding applied normal stress on the unit cell in the z-direction, denoted as σ^s, can be obtained from the following equation:

$$\tau_{nt}^c = \frac{\beta R_{nt}}{2}\frac{k_3}{k_2}\sigma^s \cdot \frac{\sinh(\beta l_{nt}/2)}{\cosh(\beta l_{nt}/2)} = \frac{\beta R_{nt}}{2}\frac{k_3}{k_2}\sigma^s \cdot \tanh(\beta l_{nt}/2) \tag{3.45}$$

Therefore,

$$\sigma^s = \frac{\tau_{nt}^c}{c \cdot \tanh(\beta l_{nt}/2)} \tag{3.46}$$

where $c = \beta R_{nt} k_3 / 2k_2$. The average absolute value of shear stress on the CNT when the CNT starts to slide, denoted as $\tilde{\tau}^s$, is

$$\tilde{\tau}^s = \frac{2}{l_{nt}} \int_0^{l_{nt}/2} \left|\tau_{nt}(z)\right| dz = c\sigma^s \cdot [1 - \sec h(\beta l_{nt}/2)]/(\beta l_{nt}/2) \tag{3.47}$$

As the slip between the CNT and sheath starts, the shear stress on the debonded portion of the interface remains equal to the value of the critical CNT/sheath shear stress. CNT/sheath sliding is defined to be fully developed when the average shear stress along the z-direction on the CNT reaches the critical value, $\tilde{\tau}^f = \tau_{nt}^c$. Therefore the corresponding critical external loading on the unit cell in the z-direction is as follows:

$$\sigma^f = \frac{\tau_{nt}^c}{c \cdot [1 - \sec h(\beta l_{nt}/2)]/(\beta l_{nt}/2)} \tag{3.48}$$

During the development of CNT/sheath slip, the debonded length of interface increases from zero to l_{nt}. However it is quite complicated to track the detailed stress distribution along a partially debonded interface. To simplify this problem, the average normal $\tilde{\sigma}_{nt}$ and shear stresses $\tilde{\tau}_{nt}$ of the CNT during slip development are approximated by a linear interpolation of their respective values when slip starts and when slip is fully developed:

$$\tilde{\sigma}_{nt} = \tilde{\sigma}^s + (\tilde{\sigma}^f - \tilde{\sigma}^s) \cdot \frac{\sigma - \sigma^s}{\sigma^f - \sigma^s} \tag{3.49}$$

$$\tilde{\tau}_{nt} = \tilde{\tau}^s + (\tilde{\tau}^f - \tilde{\tau}^s) \cdot \frac{\sigma - \sigma^s}{\sigma^f - \sigma^s} \tag{3.50}$$

where

$$\tilde{\sigma}^s = \frac{2}{l_{nt}} \int_0^{l_{nt}/2} \frac{k_3}{k_2} \sigma^s \left[1 - \frac{\cosh(\beta z)}{\cosh(\beta l_{nt}/2)} \right] dz = \frac{k_3}{k_2} \sigma^s [1 - \frac{\tanh(\beta l_{nt}/2)}{\beta l_{nt}/2}] \tag{3.51}$$

$$\tilde{\sigma}^f = \frac{2}{l_{nt}} \int_0^{l_{nt}/2} \frac{k_3}{k_2} \sigma^f \left[1 - \frac{\cosh(\beta z)}{\cosh(\beta l_{nt}/2)} \right] dz = \frac{k_3}{k_2} \sigma^f [1 - \frac{\tanh(\beta l_{nt}/2)}{\beta l_{nt}/2}] \tag{3.52}$$

$\tilde{\sigma}^s$ is the normal stress of the CNTs when the CNT/sheath slip starts, and $\tilde{\sigma}^f$ is the normal stress of the CNTs at the point of fully developed CNT/sheath slip.

After the CNT/sheath slip is fully developed, only the resin deforms further under increasing external load because all the CNTs are debonded. The shear stresses of the CNTs are τ_{nt}^c now. Likewise, the normal stresses in the CNTs are $\tilde{\sigma}^f$.

Overall, the whole process of the deformation of the unit cell can also be defined in Table 3.4-1, besides described in Table 3.2-1, in terms of the externally applied normal stress on the unit cell in the z-direction.

Table 3.4-1 Deformation process

Applied normal stress on composite σ	**Perfectly bonded**	**CNT/sheath sliding**	**After fully debonded**
	$\sigma \le \sigma^s$	$\sigma^s < \sigma \le \sigma^f$	$\sigma > \sigma^f$

3.5 *Effective Moduli and Loss Factor of Composite*

The shear lag analysis can be used to calculate the effective longitudinal modulus of the composite. Let E_c represent the Young's modulus of the unit cell along the z-direction, the effective Young's modulus of the composite containing vertically aligned CNT can be written as:

$$E_c = \left[\tilde{\sigma}_{rs} \cdot \left(1 - \frac{\pi R_{nt}^2}{(d+2R_{nt})^2} \right) + \tilde{\sigma}_{nt} \cdot \frac{\pi R_{nt}^2}{(d+2R_{nt})^2} \right] \Big/ \tilde{\varepsilon}_c \tag{3.53}$$

where $\tilde{\sigma}_{nt}$ is the average normal stress of the CNT; if the CNT and sheath are perfectly bonded, it can be calculated by integration of equation (3.42). However, if the CNT/sheath sliding occurs, equation (3.49) should be used instead. Otherwise, equation (3.52) should be used in the case that the CNT/sheath slip is fully developed. $\tilde{\sigma}_{rs}$ is the average normal stress of the resin that can be calculated from equation (3.37) with the previously calculated normal stresses in the CNT. $\tilde{\varepsilon}_c$ is the normal strain of the composite in the z-direction, which is approximately equal to the normal strain of the resin, $\tilde{\varepsilon}_{rs} = \tilde{\sigma}_{rs} / E_{rs}$.

The loss factor is defined as the ratio of the dissipated energy as a result of damping during one cycle to the total energy of the vibration system under cyclic loading. There are two contributions of energy dissipation in the composite containing vertically aligned CNT: one is the energy loss due to "stick-slip" motion between CNT and sheath, the other is the energy dissipation in the viscoelastic resin itself.

To determine the energy loss due to the "stick-slip" motion, it has been proposed [Kelly, 1970] that the dissipated energy due to friction is equivalent to the frictional shear force times the differential displacement at the interface. When the slippage occurs, the difference in longitudinal displacements between CNT and sheath is approximated as $l^{eff} \cdot (\tilde{\varepsilon}_{rs} - \tilde{\varepsilon}_{nt})$, where l^{eff} is the effective length of the slippage, which is estimated by linear interpolation with applied stress as:

$$l^{eff} = l_{nt} \cdot \frac{\sigma - \sigma^s}{\sigma^f - \sigma^s} \tag{3.54}$$

The values of $\tilde{\varepsilon}_{rs}$ and $\tilde{\varepsilon}_{nt}$ denote the average longitudinal strain of the sheath and CNT during the slippage, respectively. They are calculated from the corresponding average normal stresses using the constitutive relationship between stress and strain:

$$\tilde{\varepsilon}_{rs} = \tilde{\sigma}_{rs} / E_{rs}, \tilde{\varepsilon}_{nt} = \tilde{\sigma}_{nt} / E_{eq} \tag{3.55}$$

The energy dissipation before the "stick-slip" motion occurs is only caused by resin itself because the CNTs are perfectly bonded with the sheath. However, the energy dissipation associated with the CNT/sheath sliding due to loading is:

$$\Delta W_s = \tau_{nt}^c \cdot 2\pi R_{nt} (l^{eff})^2 \cdot (\tilde{\varepsilon}_{rs} - \tilde{\varepsilon}_{nt}) \tag{3.56}$$

But if the CNT/sheath sliding is fully developed,

$$\Delta W_f = \tau_{nt}^c \cdot 2\pi R_{nt} (l_{nt})^2 \cdot (\tilde{\varepsilon}_{rs}{}' - \varepsilon^f) \tag{3.57}$$

where $\tilde{\varepsilon}_{rs}'$ is the average longitudinal strain of the resin on condition that the CNT/sheath slip is fully developed. ε^f is the longitudinal strain of the CNT at the point of fully developed CNT/sheath slip, which can be derived by $\varepsilon^f = \sigma^f / E_{eq}$. The energy loss from the viscoelastic material in a period can be simply derived by

$$\Delta W_r = \frac{1}{2} \int \tilde{\sigma}_{sh} \tilde{\varepsilon}_{sh} dV_{sh} \tag{3.58}$$

The effective loss factor of the composite containing vertically aligned CNT associated with the CNT/sheath sliding due to loading is calculated as follows:

$$\tan \delta = \frac{\int_0^T \Delta W_s + \int_0^T \Delta W_r}{\int_0^T W} \tag{3.59}$$

but if the CNT/sheath sliding is fully developed, then

$$\tan \delta = \frac{\int_0^T \Delta W_f + \int_0^T \Delta W_r}{\int_0^T W} \tag{3.60}$$

$\int_0^T W$ denotes the total strain energy in the entire composite in a period,

$$W = \int \left(\frac{\tilde{\sigma}_{nt}^2}{2E_{eq}} + \frac{\tilde{\tau}_{nt}^2}{2G_{eq}} \right) dV_{nt} + \int \frac{\tilde{\tau}_{nt}^2}{6G_{rs}} dV_{sh} + \int \frac{\tilde{\sigma}_{rs}^2}{2E_{rs}} dV_{rs} \tag{3.61}$$

where V_{nt}, V_{sh} and V_{rs} are volumes of the CNT, sheath and the resin in the unit cell, respectively, with the values of

$$V_{nt} = \pi R_{nt}^2 l_{nt},\ V_{sh} = \pi (R_{sh}^2 - R_{nt}^2) l_{nt},\ V_{rs} = (d + 2R_{nt})^2 l_{nt} - \pi R_{nt}^2 l_{nt} \qquad (3.62)$$

3.6 Chapter Summary

To predict the energy dissipation in composites with vertically aligned multi-walled CNTs, a structural damping model of composite unit cell composed of resin, sheath and nanotube is developed. The viscoelastic resin is represented with the Maxwell model and standard solid model. The concept of "stick-slip" motion is used to describe the frictional movements at the CNT/sheath surface. The energy dissipation in the presence of "stick-slip" friction is determined.

CHAPTER FOUR

PARAMETRIC STUDY OF THE CNT COMPOSITES

In this chapter, it will be focused on parametric study based on the model, which was developed in the previous chapter. This model could be used for predicting CNT composite dynamic properties. Several factors could affect the energy dissipation ability of the CNT composite. For example,

1. Segment length of CNTs
2. Segment space of CNTs
3. Critical shear stress of the CNTs

In the following sections, the above key factors will be studied while composite energy dissipation ability is taken into consideration. Parametric studies and discussions will be given for a prediction of the general trend of the composite characteristics.

4.1 Carbon Nanotube Dimensions

The derived structural damping model is used to analyze the loss factor for composites containing vertically aligned multi-walled CNTs. The material properties obtained from the fabricated sample are listed in Table 4.1-1.

Table 4.1-1 Model parameter

CNT segment		Epoxy resin		Critical shear stress	
Length, l_{nt}	**10** μm	**Young's modulus,** E_{rs}	**3** GPa	τ_{nt}^{c}	**0.05** GPa
Radius, R_{nt}	**15** nm	**Poisson's ratio,** ν_{rs}	**0.3**	**Sheath layer**	
Shear modulus, G_g	**0.44** TPa	**Viscosity,** ηD	$15GPa \cdot s$	**Outer radius,** R_{sh}	**17** nm
Young's modulus, E_g	**1.03** TPa	**Center-to-center distance between CNTs,** $d+2R_{nt}$		$50nm$	

The CNT segment is modeled as a solid cylinder with the same length and outer radius of the nanotube. A thin sheath tube is also built in order to simulate the contact/bonding surface between CNT and matrix. This sheath layer plays a very important role in damping simulation. Previous investigations [Cooper et al., 2002; Frankland et al., 2003; Wong et al., 2003] of bonding at CNT/resin surfaces showed that the critical shear stress between multi-walled CNT and resin ranges from 35 MPa to 500 MPa. In this simulation, 50 MPa critical CNT/sheath shear stress is chosen to illustrate the composite characteristics.

Since the focus of this research is the energy dissipation caused by the interfacial friction in the CNT composites, the damping caused by resin itself is neglected. Therefore, the energy dissipation before CNT/sheath debonding is not considered because the CNTs are perfectly bonded with the sheath. The energy dissipations

associated with the CNT and sheath sliding during the loading progress will be discussed.

The predicted loss factors are plotted in Figure 4.1-1. The Maxwell model is used here and the frequency of the applied stress is 1 Hz. It should be noted that, while the loss factors are plotted from the low to high stresses to illustrate the trend, the high stress level shown in the figure might be difficult to achieve in realistic applications without failing the material. Nevertheless, since these are only case studies and the stress level may change for different combinations of material properties, and the purpose of this investigation is to understand the general trend of the composite characteristics, it is meaningful to explore such a broad stress range.

In general, there are two distinct ranges in loss factor-stress curve. The first one might be caused by the start of CNT/sheath debonding and the second one is perhaps caused by continuous sliding after all the CNTs are fully debonded. The loss factor remains low at a small stress region, and then increases greatly (CNT/sheath debonding range) before decreases continuously (after CNT/sheath are fully debonded).

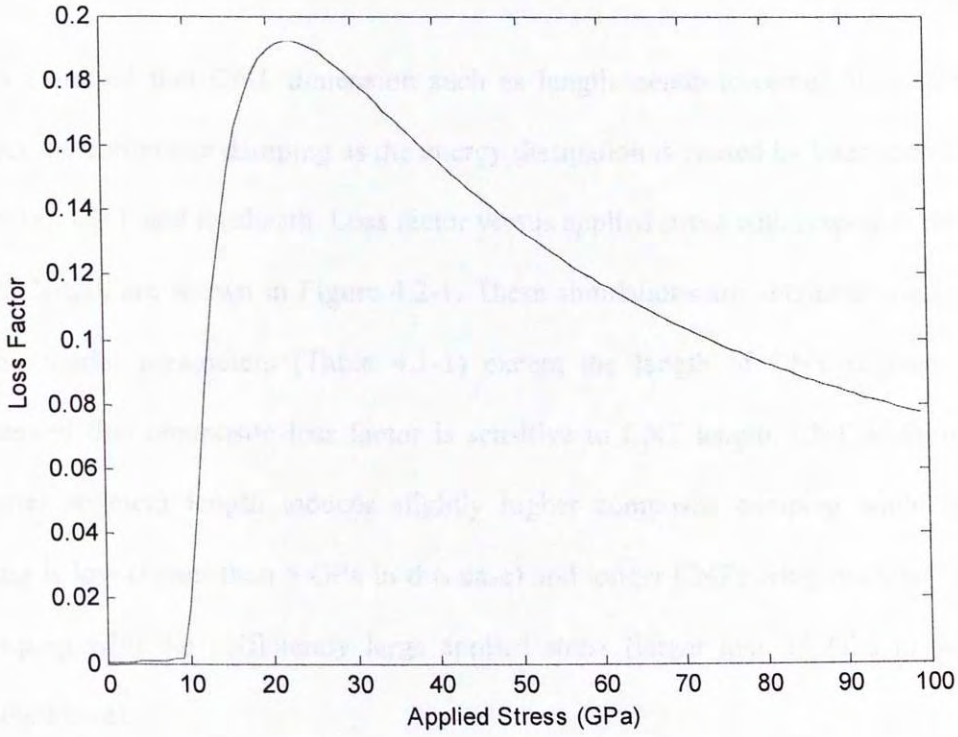

Figure 4.1-1 Loss factor vs. applied stress

4.2 Parametric Study

It is expected that CNT dimension such as length, center-to-center distance might affect the composite damping as the energy dissipation is caused by interfacial sliding between CNT and its sheath. Loss factor versus applied stress with respect to different CNT length are shown in Figure 4.2-1. These simulations are obtained based on the same model parameters (Table 4.1-1) except the length of CNT segment. It is observed that composite loss factor is sensitive to CNT length. CNT addition with shorter segment length induces slightly higher composite damping while applied stress is low (lower than 5 GPa in this case) and longer CNTs bring out much higher damping with the sufficiently large applied stress (larger than 15 GPa in the case studied here).

A similar study is performed with respect to different center-to-center distances ($d+2R_{nt}$) between CNTs. Loss factor versus applied stress with respect to different space d are shown in Figure 4.2-2. These simulations are obtained based on the same model parameters (Table 4.1-1) except the center-to-center distance of CNT segment. It can be observed from Figure 4.2-2 that the effect of center-to-center distance of CNTs on the composite loss factor is significant. More specifically, narrower space gives better composite damping performance while the applied stress is over certain level (35 GPa in the case studied here) and wider space brings out higher composite damping before this stress level.

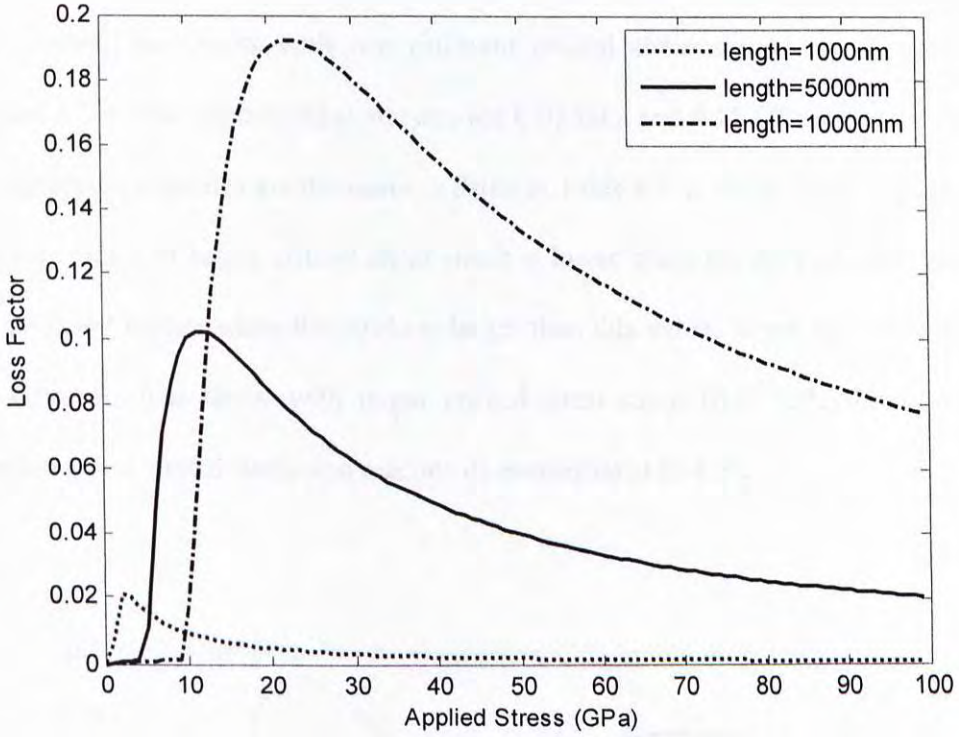

Figure 4.2-1 Loss factor vs. applied stress for composites with different segment lengths

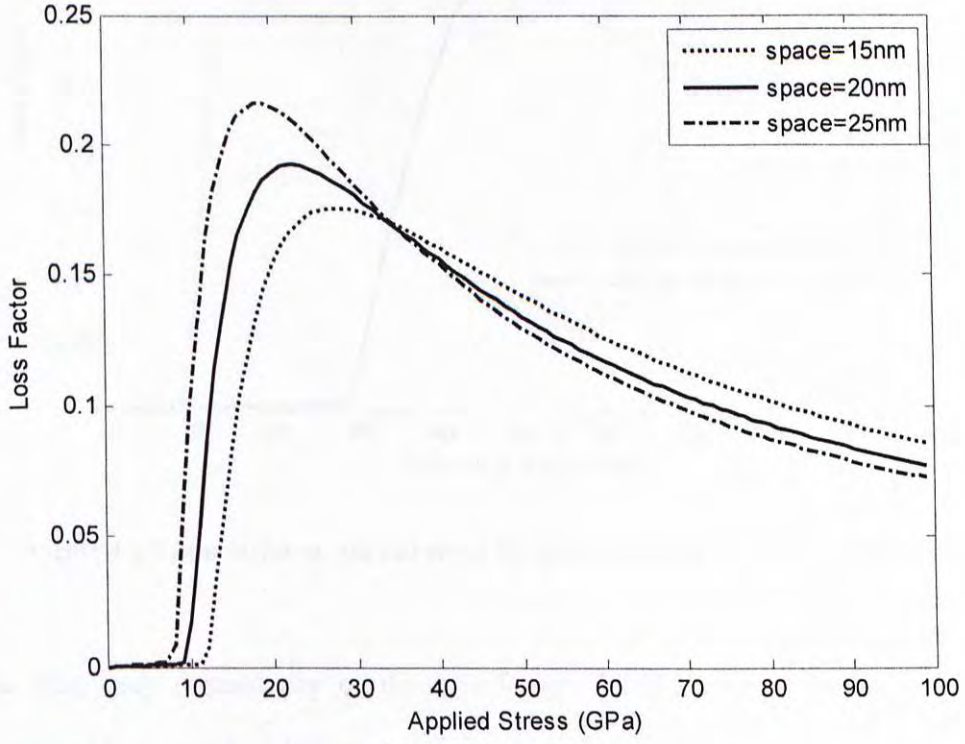

Figure 4.2-2 Loss factor vs. applied stress for composites with different segment spaces

As for the effect of critical shear stress of CNT/sheath on the damping performance of composites, the results with two different critical shear stresses are compared in Figure 4.2-4. The critical shear stresses are 0.05 GPa and 0.15 GPa, respectively, and all the other properties are the same as listed in Table 4.1-1. As shown in Figure 4.2-4, the loss factor of larger critical shear stress is lower when the applied stress is below 47 GPa and higher when the stress is larger than this value. When the stress exceeds 30 GPa, the loss factor with larger critical shear stress (0.15 GPa) increases with applied stress significantly and reaches its maximum at 65 GPa.

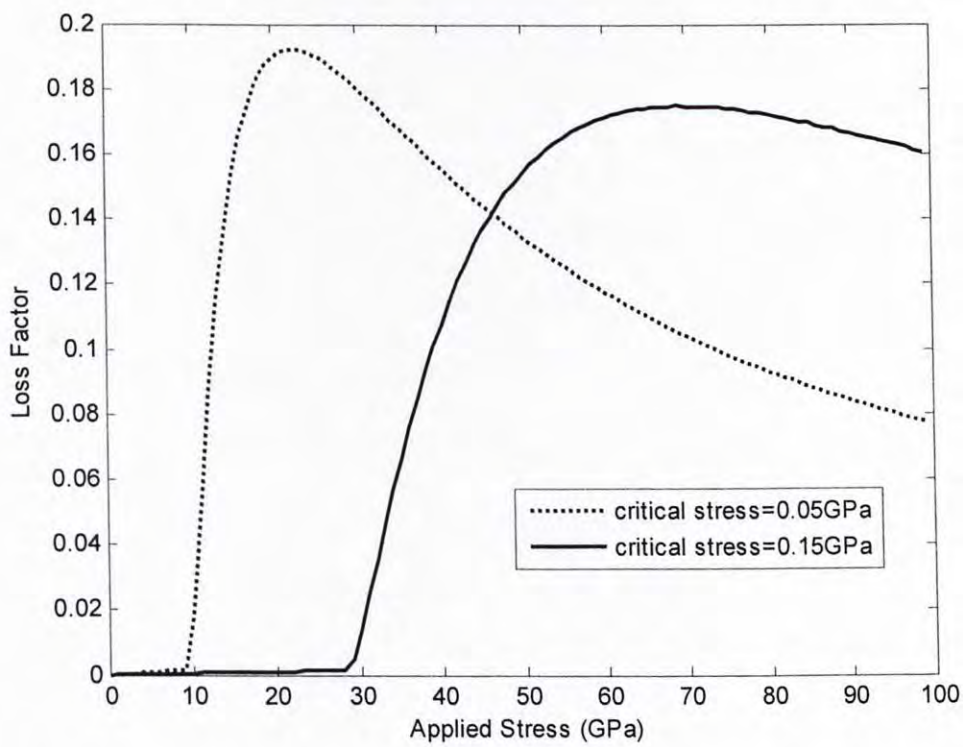

Figure 4.2-3 Loss factor vs. applied stress for composites with different critical stresses

The frequency dependency of the loss factors for the composites using Maxwell model and standard solid model is also compared. The Young's modulus and viscosities used in these two models are the same as listed in Table 4.1-1. These

parameters are chosen such that the pure viscoelastic part of these materials has identical factors at the same loading frequency. For these two models, the loss factor contribution of the "stick-slip" motion matches well in high frequency range. For instance, as the frequency of applied stress is larger than 1 Hz, the loss factor caused by interfacial friction does not change with frequency. Since the "stick-slip" motion dominates the loss factor contribution in CNT/epoxy composites, the effective loss factor can still be treated as frequency independent in high frequency range. However, the comparison of these two models in low frequency range (smaller than 1 Hz) still needs further investigation.

4.3 Summary

In order to study the damping mechanism of the CNT composite, key parameters such as CNT dimension and critical shear stress, which are expected to affect the composite damping performance, have been studied.

(1) Comparing loss factors of composites with different lengths of CNT segments, the results could vary with the applied stress. It can be predicted that if the applied stress is high enough to cause complete sliding of all the nanotubes, composites with longer length of CNT segments will provide a higher loss factor and energy dissipation capability.

(2) Due to the "stick-slip" motion, the loss factor of the composites with different center-to-center distance of CNT segments is sensitive to the applied stress. Compared to composites with narrower center-to-center distance of CNT segments, the one with wider space produces more significant damping performance at a lower stress region, and its damping ability becomes smaller when the applied stress is sufficiently high.

(3) Composites with different critical CNT/sheath shear stress start to slip at different applied stresses. Compared to composites with larger critical stress, the loss factor of composite with smaller critical stress starts to increase at a lower applied stress.

CHAPTER FIVE

CONCLUSIONS AND FUTURE WORK

5.1 Conclusions

In this research, the damping effect caused by CNT addition in CNT/Epoxy composite is studied. Vertically aligned multi-walled CNTs and the CNT/epoxy composites are fabricated. Structural mechanics based model is developed and analyzed. Parametric study is performed to investigate the composite loss factor.

The contributions of this thesis include:

1. Detailed procedures for fabricating CNT/Epoxy composites are given;
2. Structural mechanics based composite unit cell model is developed;
3. Parameters such as CNT segment length, CNT center-to-center distance, and CNT critical stress are investigated on the composite damping capacity.

The Scanning Electron Microscopy observation results show that the proposed fabrication method, vacuum-assisted resin infiltration method, is able to fabricate CNT/epoxy composites by infiltrating epoxy resins into a stack of aligned multiwalled CNT sheets to achieve homogeneous dispersion, controlled orientation and high CNT content while none of previous experiments achieved

A structural mechanics based composite unit cell model is developed, and then the loss factor of the CNT composite is calculated. It can be observed from simulation results that composite loss factor is related to stress level, and CNT dimension.

In parametric studies, several factors are discussed while composite energy dissipation ability is taken into consideration. Parameters such as CNT segment length, CNT center-to-center distance and CNT critical stress are investigated. It is found that the composite loss factor is sensitive to the mentioned parameters. The interfacial sliding developed between CNT and matrix could be categorized into three different stages (shown in Table 3.4-1) under different stress level while composite loss factor varies with different sliding stage.

5.2 Future Work

Since there is no comparison between the simulated loss factors and the experimental data, the developed model for vertically aligned carbon nanotube composites is still lack of validation. As a result, uniaxial testing is desired to be conducted so as to validate the accuracy of the simulation results.

In addition, the frequency dependency of the loss factors for the composites using Maxwell model and three-parameter standard solid model is compared. For these two models, the loss factor contributions of the "stick-slip" motion match well in high frequency range. For instance, as the frequency of applied stress is larger than 1 Hz, the loss factor due to deformation in the viscoelastic material decreases as the applied frequency increases; while loss factor caused by interfacial friction does not change with frequency. Since the "stick-slip" motion dominates the loss factor contribution in CNT-based composites, the total effective loss factor can be still treated as frequency independent in high frequency range. However, the comparison of these two models in low frequency range (smaller than 1 Hz) still needs further investigation.

Furthermore, the hybrid vibration damping combining active control (by using smart materials such as piezoelectric actuators) and CNT composites may be very effective as CNT composites can provide significant damping as well as high stiffness.

BIBLIOGRAPHY

Ajayan, P. M., Stephan, O., Colliex, C., and Trauth, D., "Aligned Carbon Nanotube Arrays Formed by Cutting a Polymer Resin-Nanotube Composite," Science, Vol.265, pp.1212-1215, 1994

Baughman, R. H., Zakhidov, A. A., and Walt, A., "Carbon Nanotubes – the Route toward Applications," Science, Vol.297, pp.787-792, 2002

Biggerstaff, J., and Kosmatka, J., "Damping Performance of Cocured Viscoelastic Composite Laminates with Embedded Viscoelastic Layer," Journal of Composite Materials, Vol.32 (21), pp.1-14, 1998

Brackbill, C., Ruhl, L., Lesieutre, G., and Smith, E., "Characterization and Modeling of the Low Strain Amplitude and Frequency Dependent Behavior of Elastomeric Damper Materials," Journal of the American Helicopter Society, Vol.45 (1), pp.34-42, 2000

Buldum, A., and Lu, J. P., "Atomic Scale Sliding and Rolling of Carbon Nanotubes," Physics Review Letters, Vol.83, pp.5050-5053, 1999

Cantoro, M. and Hofmann, S., "Catalytic Chemical Vapor Deposition of Sing-wall Carbon Nanotubes at Low Temperatures," Nano Letters, Vol.6 (6), pp.1107-1112, 2005

Chiang, I. W., Brinson, B. E., Smalley, R. E., Margrave, J. L., and Hauge, R. H., "Purification and Characterization of Single-wall Carbon Nanotubes," Journal of Physical Chemistry B, Vol.105, pp.1157-1161, 2001

Cooper, C. A., Cohen, S. R., Barber, A. H., and Wagner, H. D., "Detachment of Nanotubes from a Polymer Matrix," Applied Physics Letters, 81(20): 3873-3875, 2002

Dai, R. L., and Liao, W. H., "Modeling of Carbon Nanotube Composites for Vibration Damping," Proceedings of SPIE Conference on Smart Structures and Materials, SPIE Vol. 6528, 2007

Frankland, S. J. V., Bandorawalla, T., and Gates, T. S., "Calculation of Non-bonded Forces Due to Sliding of Bundled Carbon Nanotubes," Proceedings of 44 th AIAA/ASME/ASCE/AHS/ASC Structures, Structural Dynamics, and Materials Conference, Vol.2, AIAA, Reston, VA, pp. 1252-1262, 2003

Gojny, F. H., Wichmann, M. H. G., Fiedler, B., and Schulte, K., "Influence of Different Carbon Nanotubes on the Mechanical Properties of Epoxy Matrix Composites – A Comparative Study," Composite Science Technology, Vol.65, pp.2300-2303, 2005

Holscher, H., Schwarz, U. D., Zworner, O., and Wiesendanger, R., "Consequences of the Stick-slip Movement for the Scanning Force Microscopy Imaging of Graphite," Physics Review B, Vol.57, pp.2477-2481, 1998

Iijima, S., "Helical Microtubules of Graphitic Carbon," Nature, Vol.354 (56), pp.56-58, 1991

Kabir, M., S. and Morjan, R. E., "Plasma-enhanced Chemical Vapor Deposition Growth of Carbon Nanotubes on Different Metal Underlayers," Nanotechnology, Vol.16, pp.458-466, 2005

Kelly, A., "Interface Effects and the Work of Fibrous Composites," Proceedings of Royal Society Lond A, Vol.344, pp.287-302, 1970

Koratkar, N., Wei, B., and Ajayan, P. M., "Multifunctional Structural Reinforcement Featuring Carbon Nanotube Films," Composites Science and Technology, Vol.63, pp.1525-1531, 2003

Liu, A., Wang, K. W., Bakis, C. E., and Huang, J. H., "Analysis of Damping Characteristics of a Viscoelastic Polymer Filled with Randomly Oriented Sing-Wall Nanotube Ropes," Proceedings of SPIE International Symposium on Smart Structures and Materials, SPIE, Vol.6169, pp.275-291, 2006

Meyyappan, M. and Delzeit, L., "Carbon Nanotube Growth by PECVD: a Review," Plasma Sources Science and Technology, Vol.12, pp.205-216, 2003

Moniruzzaman, M., and Winey, K. I., "Polymer Nanocomposites Containing Carbon Nanotubes," Macromolecules, Vol.39, pp.5194-5196, 2006

Odegard, G. M., Gates, T. S., Nicholson, L. M., and Wise, K. E., "Equivalent Continuum Modeling of Nanostructured Materials," NASA/TM-2001-210863, 2001

Qian, D., Wagner, G. J., Liu, W. K., Yu, M. F., and Ruoff, R. S., "Mechanics of Carbon Nanotubes," Applied Mechanics Review, Vol.55 (6), pp.495-533, 2002

Ru, C. Q., "Effect of van der Waals Forces on Axial Buckling of a Double-walled Carbon Nanotube," Journal of Applied Physics, Vol.87(10), pp.7227-7231, 2000

Salvetat, J. P., Bonard, J. M., Thomson, N. H., Kulik, A. J., Forro, L., Benoit, W., and Zuppiroli, L., "Mechanical Properties of Carbon Nanotubes," Applied Physics A, Material Science and Processing, Vol.69, pp.255-260, 1999

Shames, I. H., and Cozzarelli, F. A., 1991. Elastic and Inelastic Stress Analysis, Prentice Hall

Thostenson, E. T., Ren, Z. F., and Chou, T. W., "Advances in the Science and Technology of Carbon Nanotubes and Their Composites: A Review," Composites Science and Technology, Vol.61 (13), pp.1899-1912, 2001

Treacy, M. M. J., Ebbesen, T. W., and Gibson, J. M., "Exceptionally High Young's Modulus Observed for Individual Carbon Nanotubes," Nature, Vol.381, pp.678-680, 1996

Wang, Z., Liang, Z. Y., Wang, B., Zhang, C., and Kramer, L., "Processing and Property Investigation of Single-walled Carbon Nanotube (SWNT) Buckypaper/Epoxy Resin Matrix Nanocomposites," Composites Part A, Vol.35, pp.1225-1227, 2004

Wong, E. W., Sheehan, P. E., and Lieber, C. M., "Nanobeam Mechanics: Elasticity, Strength, and Toughness of Nanorods and Nanotubes," Science, Vol.277, pp.1971-1975, 1997

Wong, M., Paramsothy, M., Xu, X. J., Ren, Y., Li, S., and Liao, K., "Physical Interaction at Carbon Nanotube-polymer Interface," Polymer Vol.44(25), pp. 7757-7764, 2003

Yu, M. F., Yakobson, B. I., and Ruoff, R. S., "Controlled Sliding and Pullout of Nested Shells in Individual Multi-walled Carbon Nanotubes," Journal of Physical Chemistry B, Vol.104 (37), pp.8764-8767, 2000

Zhou, X., Shin, E., Wang, K. W., and Bakis, C., "Damping Characteristics of Nanotube Enhanced Composites," Proceedings of ASME Design Engineering Technical Conference, DETC2003/VIB-48637, Chicage, IL, 2003

Zhu, J., Peng, H. Q., Rodriguez-Macias, F., Margrave, J. L., Khabasheskku, V. N., Imam, A. M., Lozano, K., and Barrera, E. V., "Reinforcing Epoxy Polymer Composites through Covalent Integration of Functionalized Nanotubes," Advanced Functional Materials, Vol.14, pp. 643-645, 2004

Zhu, W., Jin, S., and Zhou, O., "Plasma-induced Alignment of Carbon Nanotubes," Applied Physics Letters, Vol.77 (6), pp.830-832, 2000

APPENDIX

A. Epoxy Resin Datasheet

NORLAND PRODUCTS

2540 Route 130, Suite 100, P.O. Box 637, Cranbury, NJ 08512
Tel. (609) 395-1966 Fax (609) 395-9006

1. PRODUCT INFORMATION

TRADE NAME: Norland Optical Adhesive 84

SYNONYMS: NOA 84

PRODUCT USE: Ultraviolet Cure Adhesive

HEALTH	Moderate
FLAMMABILITY	Moderate
REACTIVITY	Moderate
PROTECTIVE	Gloves & Eye Protection

2. HAZARDOUS COMPONENTS

COMPONENTS	CAS#	CONCENTRATION	OSHA PEL	ACGIH TLV	LD50	LC50
Aliphatic Urethane Acrylate*	*	65-90%	NE	NE	NAv	NAv
Isobornyl Acrylate	5888-33-5	10-30%	NE	NE	NAv	NAv
1,6 Hexanediol Diacrylate	13048-33-4	5-15%	NE	NE	NAv	NAv
Flourester	352-87-4	1-5%	NE	NE	NAv	NAv

NA=Not Applicable NAv=Not Available NE=Not Established

* The specific chemical identity and concentration is being withheld from this data sheet as a Trade Secret. None of the ingredients are listed as carcinogens in NTP, IARC or OSHA or any state's list of chemicals known to cause reproductive toxicity

3. PHYSICAL DATA

BOILING POINT (℃): NA

SPECIFIC GRAVITY (H20=1): 1.1

VAPOR PRESSURE (mm Hg): <0.1 @ 20℃

PHYSICAL STATE: Liquid

VAPOR DENSITY (AIR=1): >1

EVAPORATION RATE: <Butyl Acetate

PH: NA

PERCENT VOLATILE BY VOLUME: <.1

ODOR THRESHOLD (ppm): NAv

FREEZING POINT (℃): NAv

ODOR AND APPEARANCE: Acrylic odor. Yellow tint…

SOLUBILITY IN WATER: Not soluble

Typical Properties of NOA 84	
Refractive Index	1.46
Temperature Range	-15 C to 90° C
Viscosity @ 25C	40 to 75 cps
Elongation at Failure	57 %
Modulus of Elasticity (psi)	1,140
Tensile Strength (psi)	649
Hardness - Shore D	55

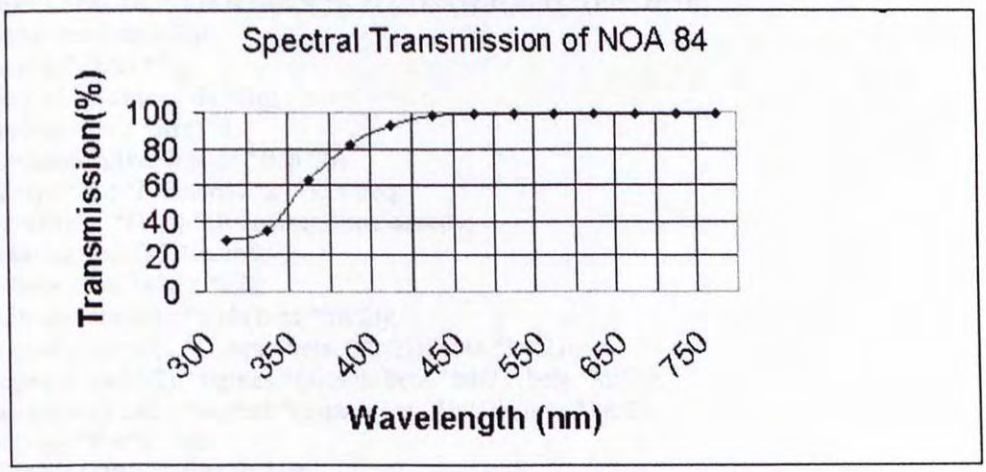

B. Matlab Program for Young's Modulus Calculation

```
function modulus()
clear
clc

Ec=[];
for t=0:0.0001:0.25;
   lnt=41300;
   Rnt=15;
   Gg=440;
   Eg=1030;
   Ers=3;
   vrs=0.3;
   Rsh=17;
   thickness=10;
   d=20;
   tauntc=0.16;
   elta=2.5;
   sigma0=200;
   la=50000;

   sigma=sigma0.*sin(2.*pi.*t);

   K=Ers.*elta/((3.*Ers+3.*elta)-vrs.*(6.*Ers+6.*elta));
   Grs=3.*elta.*K.*Ers/(9.*K.*Ers+9.*K.*elta-Ers.*elta);

% K=-Ers.*(Ers+elta)/(6.*(2.*Ers+elta).*(vrs-0.5));
% Grs=3.*Ers.*K.*(Ers+elta)/(9.*K.*(2.*Ers+elta)-Ers.*(Ers+elta));
   alpha=thickness/Rnt;
   Eeq=2.*alpha.*Eg;
   Geq=(1-(1-alpha)^4).*Gg;
   lambda=(d+2.*Rnt)^2;
   k3=lambda/(lambda-pi.*Rsh^2);
   k2=(pi.*Rnt^2/lambda).*k3+Ers/Eeq;
   k1=(Ers/(2.*Grs)).*(Rsh-Rnt).*Rnt/lambda;
   beta=sqrt(k2/(k1.*lambda));
   c=beta.*Rnt.*k3/(2.*k2);
   sigmas=tauntc/(c.*tanh(beta.*lnt/2));
   sigmaf=tauntc/(c.*(1-sech(beta.*lnt/2))/(beta.*lnt/2));
   sigmas1=(k3/k2).*sigmas.*(1-tanh(beta.*lnt/2)/(beta.*lnt/2));
   sigmaf1=(k3/k2).*sigmaf.*(1-tanh(beta.*lnt/2)/(beta.*lnt/2));
   Vnt=pi.*Rnt^2.*lnt;
   Vsh=pi.*(Rsh^2-Rnt^2).*lnt;
   Vrs=(d+2.*Rnt)^2.*lnt-pi.*Rnt^2.*lnt;
   taus1=c.*sigmas.*(1-sech(beta.*lnt/2))/(beta.*lnt/2);
   tauf1=tauntc;

   for k=1:length(t)
      if(sigma(k)<=sigmas)
         Q1=quadl(@(z)hanshu1(z,k3,k2,sigma(k),beta,lnt),0,lnt/2);
         sigmant1(k)=(2/lnt).*Q1;
      end

      if((sigmas<sigma(k))&(sigma(k)<=sigmaf))
         sigmant1(k)=sigmas1+(sigmaf1-sigmas1).*(sigma(k)-sigmas)/(sigmaf-sigmas);
```

```
    end

    if(sigma(k)>sigmaf)
      sigmant1(k)=sigmaf1;
    end
  end

  sigmars1=(sigma.*(d+2.*Rnt)^2-pi.*Rnt^2.*sigmant1)/((d+2.*Rnt)^2-pi.*Rsh^2);
  epsilongrs1=sigmars1/Ers;
  Ec=[Ec (sigmars1.*(1-
pi.*Rnt^2.*lnt/((d+2.*Rnt)^2.*la))+sigmant1.*pi.*Rnt^2.*lnt/((d+2.*Rnt)^2.*la))/epsilongrs1];

end

t=0:0.0001:0.25;
sigma0=200;
sigma=sigma0.*sin(2.*pi.*t);
plot(sigma,Ec,'LineWidth',2)
xlabel('Applied Stress (GPa)')
ylabel('Loss Factor')
end

function y=hanshu1(z,k3,k2,sigma,beta,lnt)
y=abs((k3/k2).*sigma.*(1-cosh(beta.*z)/cosh(beta.*lnt/2)));
end
```

C. Matlab Program for Loss Factor Calculation

```
function loss()
clear
clc

sigma0=0.1:1:200;
for k=1:length(sigma0)
   k
   Q3=quad(@(t)Integ1(t,sigma0(k)),0,1);
   Q4=quad(@(t)Integ2(t,sigma0(k)),0,1);
   factor(k)=1-Q3/Q4
end
plot(sigma0,factor)
end

function y=hanshu1(z,k3,k2,sigma,beta,lnt)
y=abs((k3/k2)*sigma*(1-cosh(beta*z)/cosh(beta*lnt/2)));
end

function y=hanshu2(z,k3,k2,sigma,beta,Rnt,lnt)
y=abs(beta*(Rnt/2)*(k3/k2)*sigma*sinh(beta*z)/cosh(beta*lnt/2));
end

function y=Integ1(t,sigma0)

lnt=41300;
Rnt=15;
Gg=440;
Eg=1030;
Ers=3;
vrs=0.3;
Rsh=17;
thickness=10;
d=20;
tauntc=0.16;
elta=2.5;
la=50000;
sigma=sigma0*sin(2*pi*t);

K=Ers*elta/((3*Ers+3*elta)-vrs*(6*Ers+6*elta));
Grs=3*elta*K*Ers/(9*K*Ers+9*K*elta-Ers*elta);
%K=-Ers*(Ers+elta)/(6*(2*Ers+elta)*(vrs-0.5));
%Grs=3*Ers*K*(Ers+elta)/(9*K*(2*Ers+elta)-Ers*(Ers+elta));

alpha=thickness/Rnt;
Eeq=2*alpha*Eg;
Geq=(1-(1-alpha)^4)*Gg;
lambda=(d+2*Rnt)^2;
k3=lambda/(lambda-pi*Rsh^2);
k2=(pi*Rnt^2/lambda)*k3+Ers/Eeq;
k1=(Ers/(2*Grs))*(Rsh-Rnt)*Rnt/lambda;
beta=sqrt(k2/(k1*lambda));
c=beta*Rnt*k3/(2*k2);
sigmas=tauntc/(c*tanh(beta*lnt/2));
sigmaf=tauntc/(c*(1-sech(beta*lnt/2))/(beta*lnt/2));
```

```
sigmas1=(k3/k2)*sigmas*(1-tanh(beta*lnt/2)/(beta*lnt/2));
sigmaf1=(k3/k2)*sigmaf*(1-tanh(beta*lnt/2)/(beta*lnt/2));
Vnt=pi*Rnt^2*lnt;
Vsh=pi*(Rsh^2-Rnt^2)*lnt;
Vrs=(d+2*Rnt)^2*la-pi*Rnt^2*lnt;
taus1=c*sigmas*(1-sech(beta*lnt/2))/(beta*lnt/2);
tauf1=tauntc;

for k=1:length(t)
  if(sigma(k)<=sigmas)
    leff(k)=0;
    Q1=quad(@(z)hanshu2(z,k3,k2,sigma(k),beta,Rnt,lnt),0,lnt/2);
    taunt1(k)=(2/lnt)*Q1;
    Q2=quad(@(z)hanshu1(z,k3,k2,sigma(k),beta,lnt),0,lnt/2);
    sigmant1(k)=(2/lnt)*Q2;
  end

  if((sigmas<sigma(k))&(sigma(k)<=sigmaf))
    leff(k)=lnt*(sigma(k)-sigmas)/(sigmaf-sigmas);
    taunt1(k)=taus1+(tauf1-taus1)*(sigma(k)-sigmas)/(sigmaf-sigmas);
    sigmant1(k)=sigmas1+(sigmaf1-sigmas1)*(sigma(k)-sigmas)/(sigmaf-sigmas);
  end

  if(sigma(k)>sigmaf)
    leff(k)=lnt;
    taunt1(k)=tauntc;
    sigmant1(k)=sigmaf1;
  end
end

sigmars1=(sigma*(d+2*Rnt)^2-pi*Rnt^2*sigmant1)/((d+2*Rnt)^2-pi*Rsh^2);
epsilongrs1=sigmars1/Ers;
epsilongnt1=sigmant1/Eeq;
dWnt=tauntc*2*pi*Rnt*leff.^2.*(epsilongrs1-epsilongnt1);
dWeq=Vrs*sigmars1.^2/(2*Ers);
y=dWeq;
end

function y=Integ2(t,sigma0)
lnt=41300;
Rnt=15;
Gg=440;
Eg=1030;
Ers=3;
vrs=0.3;
Rsh=17;
thickness=10;
d=20;
tauntc=0.16;
elta=2.5;
la=50000;
sigma=sigma0*sin(2*pi*t);

K=Ers*elta/((3*Ers+3*elta)-vrs*(6*Ers+6*elta));
Grs=3*elta*K*Ers/(9*K*Ers+9*K*elta-Ers*elta);
% K2=-Ers*(Ers+elta)/(6*(2*Ers+elta)*(vrs-0.5));
% Grs2=3*Ers*K2*(Ers+elta)/(9*K2*(2*Ers+elta)-Ers*(Ers+elta));
```

```
alpha=thickness/Rnt;
Eeq=2*alpha*Eg;
Geq=(1-(1-alpha)^4)*Gg;
lambda=(d+2*Rnt)^2;
k3=lambda/(lambda-pi*Rsh^2);
k2=(pi*Rnt^2/lambda)*k3+Ers/Eeq;
k1=(Ers/(2*Grs))*(Rsh-Rnt)*Rnt/lambda;
beta=sqrt(k2/(k1*lambda));
c=beta*Rnt*k3/(2*k2);
sigmas=tauntc/(c*tanh(beta*lnt/2));
sigmaf=tauntc/(c*(1-sech(beta*lnt/2))/(beta*lnt/2));
sigmas1=(k3/k2)*sigmas*(1-tanh(beta*lnt/2)/(beta*lnt/2));
sigmaf1=(k3/k2)*sigmaf*(1-tanh(beta*lnt/2)/(beta*lnt/2));
Vnt=pi*Rnt^2*lnt;
Vsh=pi*(Rsh^2-Rnt^2)*lnt;
Vrs=(d+2*Rnt)^2*la-pi*Rnt^2*lnt;
taus1=c*sigmas*(1-sech(beta*lnt/2))/(beta*lnt/2);
tauf1=tauntc;

for k=1:length(t)
   if(sigma(k)<=sigmas)
      leff(k)=0;
      Q1=quad(@(z)hanshu2(z,k3,k2,sigma(k),beta,Rnt,lnt),0,lnt/2);
      taunt1(k)=(2/lnt)*Q1;
      Q2=quad(@(z)hanshu1(z,k3,k2,sigma(k),beta,lnt),0,lnt/2);
      sigmant1(k)=(2/lnt)*Q2;
   end

   if((sigmas<sigma(k))&(sigma(k)<=sigmaf))
      leff(k)=lnt*(sigma(k)-sigmas)/(sigmaf-sigmas);
      taunt1(k)=taus1+(tauf1-taus1)*(sigma(k)-sigmas)/(sigmaf-sigmas);
      sigmant1(k)=sigmas1+(sigmaf1-sigmas1)*(sigma(k)-sigmas)/(sigmaf-sigmas);
   end

   if(sigma(k)>sigmaf)
      leff(k)=lnt;
      taunt1(k)=tauntc;
      sigmant1(k)=sigmaf1;
   end
end

sigmars1=(sigma*(d+2*Rnt)^2-pi*Rnt^2*sigmant1)/((d+2*Rnt)^2-pi*Rsh^2);
epsilongrs1=sigmars1/Ers;
epsilongnt1=sigmant1/Eeq;
W=(sigmant1.^2/(2*Eeq)+taunt1.^2/(2*Geq))*Vnt+Vsh*taunt1.^2/(6*Grs)+Vrs*sigmars1.^2/(2*
Ers);
y=W;

end
```